

Calibrating HPT-profiles with micro-CT scans using upscaling from pore to field scale

Master's Thesis

Wout Hanckmann
5512778

Supervisors:
dr. Alraune Zech, UU
Msc. Marloes van Lipzig, Inpijn-Blokpoel Ingenieurs

External advisor:
dr. Willem-Bart Bartels, Lievense Adviseurs Ingenieurs

Environmental Hydrogeology Group
Department of Earth Sciences
Faculty of Geosciences
January 2021

Abstract

The potential of calibrating HPT-profiles with micro-CT scans using upscaling from pore-scale to field-scale has been investigated. Undisturbed samples ranging from clayey silt to fine sand have been retrieved along a 9m deep HPT-profile and taken to the laboratory. Kapton® polyimide tubes ranging from 3-5mm were pushed into the cores and sealed on both sides for micro-CT scanning with a Zeiss Xradia 610 Versa with a voxel size ranging between 0.56 – 2.02 μ m. A pore-network-model was extracted from the segmented images and loaded into PoreFlow to determine absolute hydraulic conductivities.

An HPT-profile is calibrated to the results obtained with micro-CT scans and compared to 0.5 – 2m slug tests along the profiles for verification. HPT is not suited for low- K soils. Therefore, we focus our comparison between lab, field and HPT test on sandy soil types. Good results were observed when the profile is calibrated to samples obtained from a fine sand section. To expand this workflow to coarser soil types, the use of sodium silicates, known as waterglass is assessed in retrieving coarse undisturbed soil samples by gelatinizing the pore space making the sediments more cohesive. The technique shows potential in combination with micro-CT scanning as an appliance for retrieving undisturbed coarse materials from the subsurface.

Keywords: hydraulic conductivity, direct-push, HPT, micro-CT scanning, hydraulic upscaling, pore-network modelling, undisturbed samples, sodium silicate, waterglass

Contents

1. Introduction	1
2. Materials and methods.....	2
2.1. HPT profiles.....	2
2.1.1. Site location.....	2
2.1.2. HPT-profiles in general.....	3
2.1.3. Geostatistical analysis.....	4
2.2. Sample preparation	3
2.2.1. Retrieving undisturbed samples from the subsurface	3
2.2.2. The potential of sodium silicate gels	4
2.2.3. Sample preparation for micro-CT scan	4
2.3. Obtaining absolute <i>K</i> -values	5
2.3.1. Micro-CT scanning.....	6
2.3.2. Image processing.....	7
2.3.3. Generate input files pore-network-model (PNM)	8
2.3.4. Generation of PNM and programs used.....	9
2.4. HPT-calibration	10
3. Results	10
3.1. HPT profile	10
3.2. Geostatistical analysis	11
3.3. Waterglass	13
3.4. Micro-CT images + segmentation.....	13
3.5. Pore network analysis	14
3.6. HPT calibration	15
4. Discussion.....	16
4.1. Reliability of the HPT measurements	16
4.2. Geostatistical analysis	18
4.3. Retrieving undisturbed samples	18
4.4. Potential of waterglass.....	18
4.5. Micro-CT scanning	18
4.6. Modelling fluid flow	19
4.7. Calibration strategy	19
5. Conclusion	19
5.1. Further research	19
6. Acknowledgements	20
7. References.....	20

1. Introduction

The hydraulic conductivity (K) is arguably the most critical parameter for predicting groundwater flow and contaminant transport. Determining and modelling the heterogeneous structure of K under limited availability of observation data has been an unsolved subject within science for decades (Gelhar & Axness, 1983; Dagan, 1989; Boggs et al., 1992; Koltermann & Gorelick, 1996; Dagan & Neuman, 1997; Fogg et al., 2000; Butler et al., 2002; Bohling et al., 2012; Wiggers et al., 2019).

Over the past century several techniques have been developed to determine a small-scale picture of K in the field. Tracer tests furnish detailed information of the solute movement that potentially allows to infer the spatial variations of K between the observation wells (Datta-Gupta et al., 2002; Ptak et al., 2004; Butler et al., 2007), yet they are time consuming and cost-intensive. Traditional pumping tests (Butler, 2005; Leven & Dietrich, 2006) provide average K -values over large aquifer volumes, but little information concerning the local heterogeneity that is of interest for piping problems known for causing weak spots in dikes (Wiggers et al., 2019).

Direct-push (DP) based techniques appear to be a more viable option for measuring high-resolution spatial variations in K . Over the past years a set of DP-based procedures have been developed (Dietrich & Leven, 2009; McCall & Christy, 2010; Liu et al., 2012; Maliva, 2016). The technology uses hydraulic rams topped up with vehicle weight and high-frequency percussion hammers (for CPT - DP) to swiftly insert small-diameter pipes into the subsurface (Lunne et al., 2002; Butler et al., 2007; Dietrich et al., 2008).

One of the most widely used approaches is Direct-push Injection Logging (DPIL) where relative information on local K -values can be acquired by injecting water at a constant flowrate (Q) while observing the change in pressure (P) with a Hydraulic Profiling Tool (HPT) as it advances into the subsurface. The resulting local Q/P measured along the profile can be considered as a proxy for the local small-scale relative K -values. A typical vertical resolution of 1.5-2.5cm can be achieved

(Borden et al., 2020). This data could eventually be extended into a full 3d K -model using kriging (Ren et al., 2019).

The advantages of direct-push based techniques are a high resolution, relatively quick installation, easy to operate and that no material in the subsurface is removed since the small-diameter pipes push the material aside (Thornton et al., 1997) making it suitable for usage near dikes and contamination sites when attaining a detailed spatial structure of K is desired on a centimetre-scale.

The drawback of HPT is that only relative K -values are measured while calibration is highly empirical and site-dependent (Dietrich et al., 2008; Liu et al., 2009; Lessoff et al., 2010; Borden et al., 2020), impeding the technique to be used to its full potential.

More “physics” can be added to the calibration strategy by looking at processes happening at the pore-scale since it has been revealed repeatedly that large field-scale processes often depend on these small-scale processes (Held & Celia, 2001; Kechagia et al., 2002; Raouf et al., 2010; Raouf et al., 2013; Wildenschild & Sheppard, 2013;).

For pore-scale analysis retrieving undisturbed samples is essential. However, for unconsolidated sediments it has been proven to be difficult due to a series of disturbance effects such as mechanical disturbance, extrusion, transportation, storage environment and specimen preparation (Lunne et al., 1997; Lunne et al., 1998). Coarser materials are more prone to these effects making them harder to retrieve undisturbed. Some methods exist to retrieve undisturbed sand sediments. For example, in situ freezing (Yoshimi et al., 1994; Kim et al., 2018). Nevertheless, in this context the technique is not useful since freeze-thaw processes artificially increases K (Tang & Yan, 2015). Another technique is the so-called “gel-pushing” technique (Taylor et al., 2012; Umehara et al., 2015). It is a relatively novel and expensive technique using a lubricant gel to reduce friction between the tube wall and sample to minimize mechanical disturbance.

A more viable solution may be found in sodium silicate gels. Also known as waterglass. These gels are widely used in The Netherlands to dewater construction sites by temporarily

lowering the permeability of the soil layer (Littlejohn et al., [1997](#); Van der Stoel, [2001](#); Dekker et al., [2020](#)). Before injecting, the waterglass remains in solution due to the presence of sodium hydroxide causing a high pH. When the waterglass is injected the pH drops and the waterglass starts to gelatinize filling the pores (Owusu, [1982](#)). These gels are relatively cheap and could help holding the material in place when retrieved with conventional drilling techniques.

Once retrieved various methods exist to characterize 3d pore space structures from undisturbed samples. FIB-SEM (focused ion beam-scanning electron microscopy) and TEM (transmission electron microscopy) are promising techniques but are currently working on length scales that are not suitable for determining the Representative Elementary Volume (REV) needed for modelling porous fluid flow (Wildenschild & Sheppard, [2013](#)). FIB-nt is an encouraging and fast developing technique capable of mapping the pore space at micrometre to nanometre scale. Disadvantages are its destructive nature, high cost and long beam time (Bultreys et al., [2016](#)).

A more propitious technique is X-ray (micro-) computed-tomography (CT). A non-destructive technique providing high quality 3d images ranging from millimetre to centimetre-scale. The spatial resolution is limited to a few hundreds of nanometres making it suitable for REV determination and as input to various flow-and-transport models to allow simulations at the pore-scale (Wildenschild & Sheppard, [2013](#); Bultreys et al., [2016](#)). Advantages are a large active community, easily available and relatively low cost.

Multiple codes are available for fluid flow simulation in porous media. Direct fluid flow modelling such as OpenFoam® and GeoDict (Math2Market) solve numerically the Navier-Stokes equation. Advantages are the complex pore geometries it can handle however they are computationally demanding. Another popular method is Lattice-Boltzmann (LB) simulation. It simulates the motion and collision of particles on a grid. When averaged the flow approximates the Navier-Stokes equation (Blunt et al., [2013](#)). These simulations are relatively easy to code and work with

complex pore geometries but are also not computationally efficient resulting in a high computational demand.

A different approach for modelling fluid-and-transport is Pore-Network-Modelling (PNM). Although it is expected that direct flow methods will be favoured in the future, PNM shows currently better results when dealing with two-phase flow (Blunt, [2001](#); Blunt et al., [2013](#); Bultreys et al., [2016](#)). Fluid flow is modelled by solving the Hagen-Poiseuille equation on a simplified pore-network geometry consisting of pore bodies (spheres) connected by cylindrical pore throats (Raouf et al., [2013](#)). Simulations are fast and computationally efficient.

Specific objectives of this study are to add more physics to the largely empirical-based calibration methods by examining the potential of computer-tomography (CT)-scans in combination with the in-house PNM called PoreFlow (Raouf et al., [2013](#)) on undisturbed soil samples taken along an HPT-profile. The resulting absolute K -values are used as a measure for calibrating HPT-profiles.

To relate findings at the pore-scale to field-scale, an upscaling procedure is needed which will be assessed in this research. Findings at the pore-scale [mm] through micro-CT scanning and PN-modelling are linked to an HPT-profile at centimetre-scale and slug tests along the profile at decimetre/metre-scale.

2. Materials and methods

The workflow from interpreting HPT results to calibration by making use of an upscaling procedure from pore-scale to field-scale is described in this section. Undisturbed samples along an HPT-profile are taken and scanned using a micro-CT scanner to load the pore structures into a PNM to obtain absolute K -values for calibration. Also, a description of geostatistical analysis on the raw HPT data is included.

2.1. HPT profiles

2.1.1. Site location

All data has been acquired at an area of 30x30 m² located on Quaternary Age aeolian deposits in the Netherlands. The site is located near

Son, The Netherlands where the subsurface largely consists of clayey silts with sandy streaks.

A total of three HPT profiles have been made with an average spacing of 30m. In the vicinity of HPT1 (1m) undisturbed samples were retrieved and slug tests performed (Fig.1).

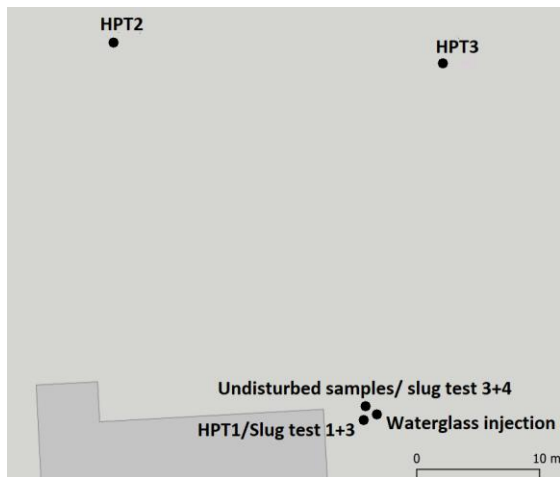


Fig. 1. A schematic map of the spatial data used in this research. A total of three HPT-profiles have been made. HPT1 is most valuable since all calibration data such as slug tests and undisturbed samples is obtained nearby (1m).

2.1.2. HPT-profiles in general

The HPT-profile is acquired using the GeoProbe system (Geoprobe, 1992; McCall et al., 2006). The HPT measures the pressure in the soil as a result of water pumped into the subsurface at the location of the HPT. The pressure measured (P_{tot}) is determined by the following factors: the pumping rate (Q), the hydraulic conductivity at the injection point (K), atmospheric pressure (P_{atm}) and hydrostatic pressure (P_{piez}). The corrected HPT pressure (P_{corr}) can be obtained with Eq 1:

$$P_{corr} = P_{tot} - (P_{piez} + P_{atm}) \quad (1)$$

With the corrected HPT pressure known, K can be estimated as a function of Q and P_{corr} according to Darcy's Law (McCall & Christy, 2020):

$$K = f(Q/P_{corr}) \quad (2)$$

The built in K -model from the GeoProbe software (Eq. 3) is based on an empirical relation between the measured Q/P_{corr} -ratio and a series of discrete interval slug tests along HPT-profiles in an alluvial aquifer located in the central USA (McCall & Christy, 2010; Geoprobe, 2010). The slug tests were performed with a pneumatic slug testing method (Butler et al., 2002) and a screen interval of 30cm. The Q/P_{corr} -profiles are averaged at depths corresponding to the screened intervals of slug test and plotted as blue diamonds in Fig. 2. The resulting empirical K -model was fitted with an R^2 of 0.83 indicating a relatively good fit. Paired HPT – slug test data from 5 other locations throughout the central USA were added for comparison.

$$Q/P_{corr} = 1.395e^{0.128K} \quad (3)$$

With Q/P_{corr} expressed in [$ml / (min \times kPa)$] and K in [m/day] transformed to SI-units.

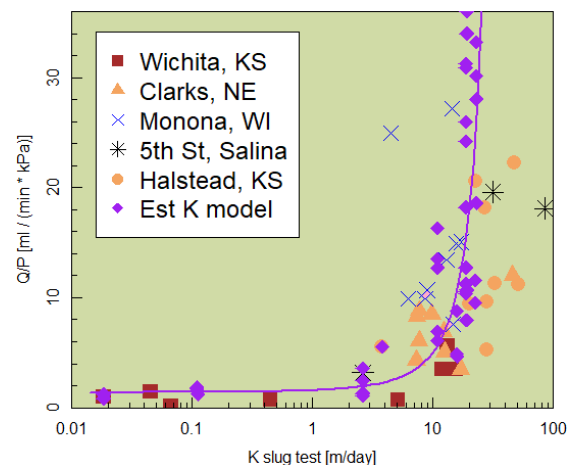


Fig. 2. From McCall and Christy, 2020. Fitting of the empirical K -model described by (McCall & Christy, 2010; Geoprobe, 2010) to paired HPT – slug test data (purple diamonds). Paired data from 5 other locations across the central US were added for comparison.

The HPT is limited in estimating K . Fig. 2 shows that K becomes highly sensitive (and probably redundant) for low Q/P_{corr} values. This can be caused by two processes. The pressure sensor of the HPT reaches the upper measurable range leading to a narrowed sensitivity, and the water may flow alternative paths of less resistance through cracks or an adjacent layer. Due to this effect with low

permeable soils, falling head tests are typically preferred over constant head tests in laboratories as it takes time for water to pass through and can be more precisely logged to obtain reliable low K -values.

The same can apply for highly permeable layers where K converges to a value around 24 m/day due to a limited sensitivity at the lower end of the pressure sensor range. Another explanation is that the slug tests are the limiting factor inhibiting the calibration for these highly conducting layers.

Hence the measurable range of K yields 3 orders of magnitude.

A more sophisticated K -model is postulated by Borden et al., 2020 (Eq. 4). This semi-

empirical model incorporates recent findings obtained by numerical modelling in COMSOL on the underlying physical processes in the subsurface during HPT-profiling (Liu et al., 2019) and was validated on 23 HPT-profiles. Novel physical parameters are the probe advancing rate V (cm/s) and probe diameter D (cm) while the injection rate Q (ml/min), corrected pressure P_{corr} (kPa) were already widely used. An empirical constant E was fitted to the HPT-data as 0.616. Note that the equation is transformed to SI units:

$$K = E (0.1235VD^2 + 0.119Q) * (0.145P_{corr})^{-1.017} \quad (4)$$

Where K is in m/day.

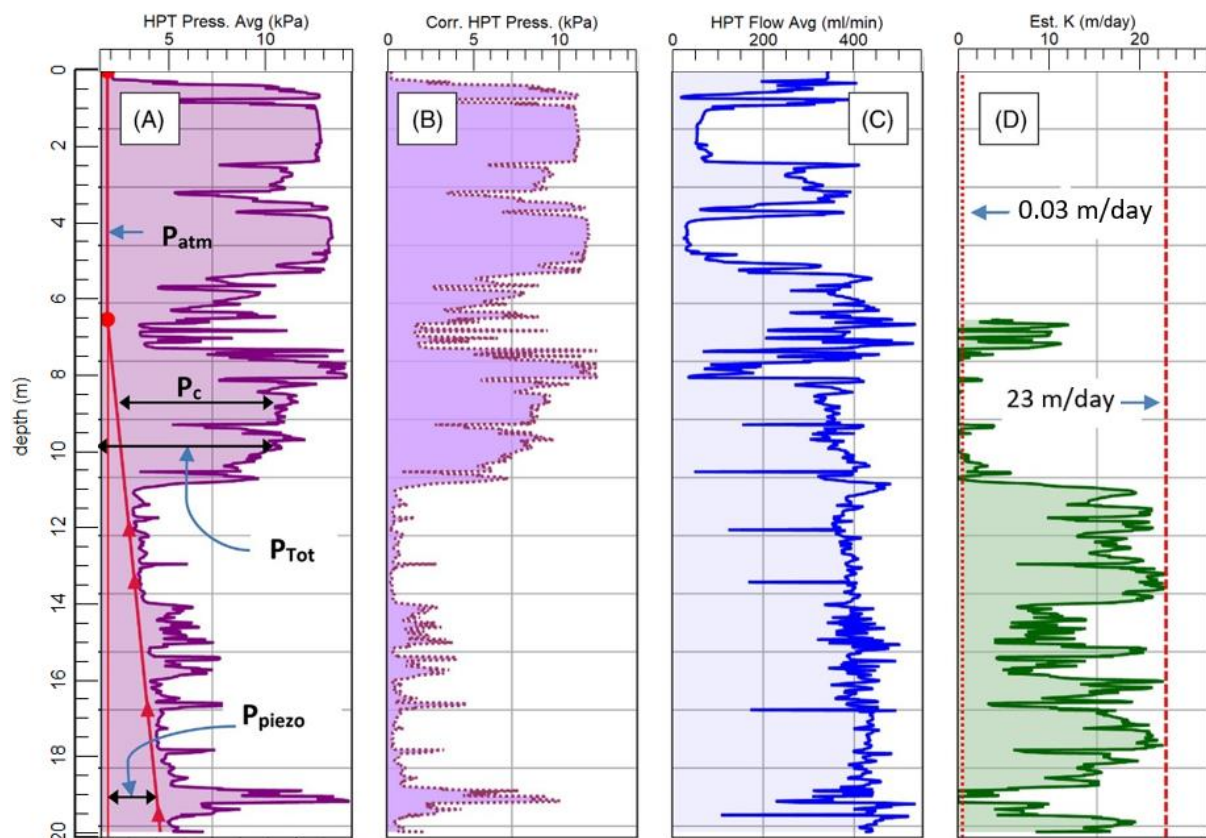


Fig. 3. From McCall and Christy, 2020. The typical output of an HPT-profile by GeoProbe®. With the total pressure (P_{tot}) and its components (Eq. 1) plotted in (A), the corrected pressure (P_{corr}) in (B), the injection flow rate (C), and (D) shows the estimated empirical K -model described by Eq. 3.

2.1.3. Geostatistical analysis

A statistical analysis will be performed on an HPT-profile to obtain one-point and two-point statistics in vertical direction. For the vertical correlation length (λ_v), a two-step approach has been used based on the Q/P_{corr} dataset.

Since HPT data tends to follow a log-normal distribution, the data is log-transformed such that it can be treated as a Gaussian stochastic process that secures stationarity (Lapidoth, 2017). After log-transformation the data is decomposed in R analogous to seasonal trend

decomposition based on Loess (STL) in timeseries analysis (Cleveland et al., 1990). It is very useful for separating data series into subseries with different length scales allowing multi-scale correlation analysis.

The decomposition makes use of Local Estimated Scatterplot Smoothing (Loess). It is a non-parametric regression technique meaning that the regression does not take a predetermined form but rather derives its form from the data. It can be determined as followed: First a weight function is determined. Traditional for Loess is the tricube weight function ($W(d)$; Eq. 5) giving more weight to data points when closer to the point of estimation.

$$W(d) = \begin{cases} (1 - |d|^3)^3 & \text{for } 0 \leq d \leq 1 \\ 0 & \text{for } d \geq 1 \end{cases} \quad (5)$$

Where d is the distance between the data point and the curve to be fitted.

A neighbourhood weight is defined using $W(d)$:

$$v_i(x) = W\left(\frac{|x_i - x|}{\lambda_q(x)}\right) \quad (6)$$

Where $\lambda_q(x)$ is the distance from q^{th} farthest x_i from x . Eq. 6 shows the x_i closest to x are more weighted. Further away from x the weights decrease and reach 0 at the q^{th} farthest point.

Finally a locally-fitted polynomial $f(x)$ of n^{th} -order is fitted through the data with weight v_i at (x_i, y_i) . Hence Loess depends on the input parameters q and n . When q becomes larger, the fitted polynomial $f(x)$ becomes smoother (Cleveland et al., 1990). The order of polynomial fitting should not exceed 2 due to overfitting the data since the idea with Loess is that simple functions can fit the data easily.

Data Y_v is decomposed into a trend (T_v), seasonal component (S_v) and a remainder (R_v). In case of decomposing a HPT-profile, the subseries are referred to a Intermediate-scale, periodic component and small-scale variations respectively.

$$R_v = Y_v - T_v - S_v \quad (7)$$

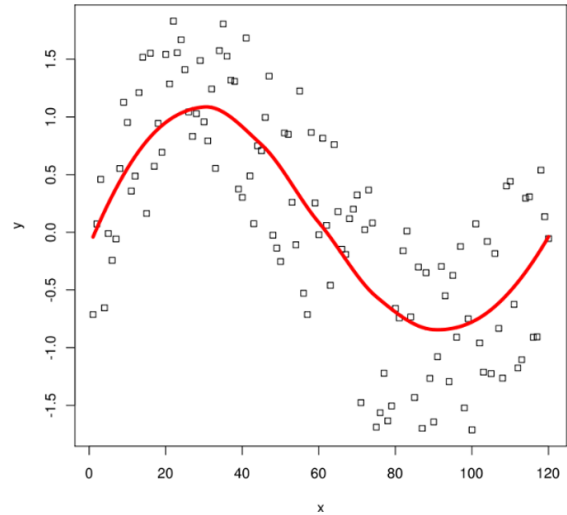


Fig. 4. From Kierano (Wikipedia): A scatterplot of a sine wave with uniform noise added. A Loess fit has been performed approximating the original sine wave.

S_v and T_v are determined through an iterative loop with $i = 2$. The loop consists of 5 steps: 1) The data series is detrended ($Y_v - T_v$). 2) Then the cyclic subseries is smoothed using Loess with $q = n_s$ and $n = 0$. 3) A low-pass filter is applied on the smoothed cyclic subseries to prevent low-frequency noise disturbing S_v . This is done by imposing a moving average and Loess smoothing with $q = n_p$ and $n = 1$. 4) The filtered seasonal component is removed from the original data ($Y_v - S_v$). 5) The remaining trend is smoothed by Loess with $q = n_t$ and $n = 1$. The q -parameter is set to default in R.

Correlation analysis is performed on the trend (T_v) and remainder (R_v) subseries by variogram fitting with the `gstat` package in R (Pebesma, 2004). A variogram (2γ) is defined as the variance of the difference between two values in a spatial random field (Eq. 8; Cressie, 2015).

$$\begin{aligned} 2\gamma(x_1, x_2) &= \text{var}(Z(x_1) - Z(x_2)) \\ &= E\left[\left((Z(x_1) - \mu(x_1)) - (Z(x_2) - \mu(x_2))\right)^2\right] \end{aligned} \quad (8)$$

Where $E[x]$ is the expected value of x . A weighted average of all possible values x could take. Z represents a random function and μ its mean. x_1 and x_2 are random locations in the field. When the field is isotropic and stationary,

the semivariogram (γ) can be simplified (Eq. 9; Cressie, 2015):

$$\gamma(x_1, x_2) = \gamma(h) \quad (9)$$

With $h = |x_2 - x_1|$ is the absolute distance between two points in the field. If the field is also ergodic meaning that all statistical properties of the field are obtained from measurements from the field itself, the limit of the semivariogram called the sill corresponds to the variance of the field (Eq. 10; Fig. 5).

$$\lim_{|x_2 - x_1| \rightarrow \infty} \gamma = \text{var}(Z(x)) \quad (10)$$

The correlation lengths are determined by fitting an autocorrelation function through a binned semivariogram. They correspond to the range of the autocorrelation function defined at a distance where the sill of the variogram is reached and the points are no longer correlated.

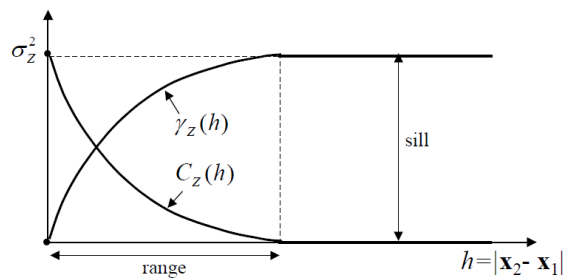


Fig. 5. A schematic plot of the semivariogram model ($\gamma_z(h)$) and covariance model ($C_z(h)$) for an ergodic isotropic stationary field Z . Note that the sill corresponds to the variance of the field.

The correlation length of the trend is expressed by λ_1 describing the thickness of the soil layers where the trend results in similar Q/P_{corr} -values while the correlation length of the remainder is expressed by λ_2 telling something about the thickness of soil layers with similar Q/P_{corr} -values at a smaller scale.

As a potential sampling/analysing method with possibilities for extension of these statistics in horizontal direction, high-resolution geostatistical subsurface models of K can be constructed analogous to an oil reservoir characterization described by Ren et al., 2019 where the average well spacing was 75m.

2.2. Sample preparation

Undisturbed samples are retrieved from the subsurface along an HPT-profile and prepared for micro-CT scanning.

2.2.1. Retrieving undisturbed samples from the subsurface

The undisturbed soil samples are retrieved by penetrating a metal casing into the subsurface while continuously injecting water to compensate for the increasing hydraulic gradient when advancing down. At the area of interest 0.5m thin-walled sample tubes with a diameter of 67mm and open on one side (Fig. 6) are hydraulically pushed into the soil and lifted out of the casing.



Fig. 6. The thin-walled sample tube of 0.5m length used for retrieving undisturbed soil samples.

The frictional drag within the sample tube holds the material in place. The sample tube is sealed and the depths are noted on both ends of the cone for transport (Fig. 7).

This procedure works well for fine materials up to fine sand. Lithologies that comprise of medium sand up to gravel are however very hard to retrieve undisturbed using this technique.

Important to note is that the retrieved soil samples range from clayey silt to fine sand with expected K -values ranging between $3E-4$ and $0,3$ m/day (Bear, 1972), meaning that we are working at the lower boundary of the K -model described in Fig. 2.

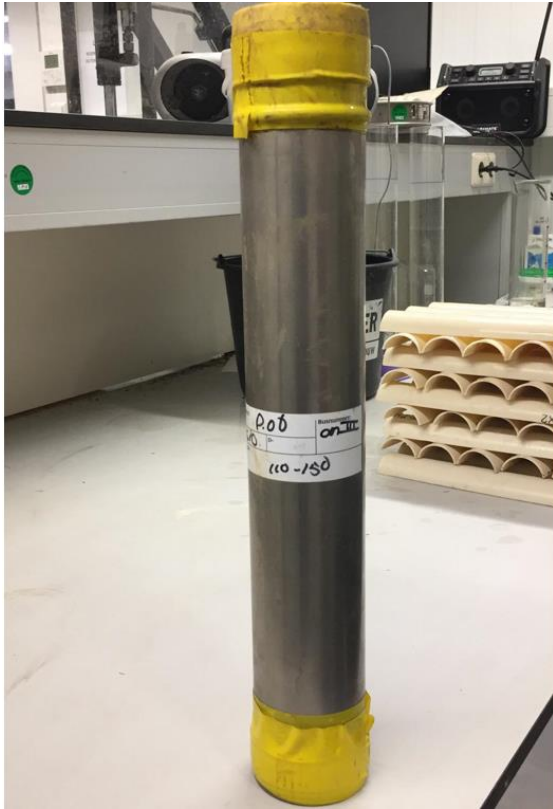


Fig. 7. A retrieved soil sample from the field brought to the lab. Both ends are sealed and the exact depth is noted.

2.2.2. The potential of sodium silicate gels

A solution may be found in sodium silicate gels, in The Netherlands often referred to as waterglass. It could help holding the undisturbed samples in place when retrieved.

To test the applicability of waterglass in combination with micro-CT scanning, 4 different waterglass mixtures are made and mixed with dry sand to test if the contrast between matrix and pore space is sufficient for reliable image segmentation. The waterglass mixtures are listed in Table 1. All mixtures are softgel mixtures (waterglass volume ratio 13%) or slightly concentrated softgels. Hardgels (waterglass volume ratio 60%) used for underwater concrete to reinforce building foundations were not tested. This due to limited CT-scan capacity and expectation that

the crystalized silica reinforcing the porous structure would show similar grey-values compared to the matrix which is mainly composed of sand (SiO_2) hindering proper image segmentation of the pore space.

Table 1. Waterglass mixtures tested for micro-CT scan contrast between matrix and pore space. The difference between soft gel and hard gel is the type of organic hardener used.

	Softgel		Hardgel	
	1	2	1	2
Waterglas %(v/v)	13.0%	24.8%	13.0%	24.8%
Esther %(v/v)	1.2%	2.3%	1.3%	2.5%
Water %(v/v)	85.8%	73.0%	85.7%	72.8%

To test the use of waterglass for retrieving undisturbed soil samples in the field, a small bulb softgel1 (Table 1) with a diameter of 1m is injected at 7m-GL (B02; Fig. 1) and left for a week to gelatinize. Then an undisturbed sample is taken as described in section 2.2.1. Since the waterglass volume ratio is low (13%), the solution is assumed to not change in volume during gelatinization.

2.2.3. Sample preparation for micro-CT scan

The retrieved soil samples are pushed out of the sample tubes onto a half-open PVC-pipes of the same diameter (Fig. 8).



Fig. 8. Undisturbed soil samples taken at B03. The samples were pushed out of the sample tube onto half-open PVC pipes.

X-ray transparent Kapton® polyimide tubes of different diameters (3mm and 5mm) and a

length of 3cm are pushed into the undisturbed samples horizontally such that the vertical CT-sample direction matches the horizontal flow direction in the subsurface during HPT-logging (Fig. 9).

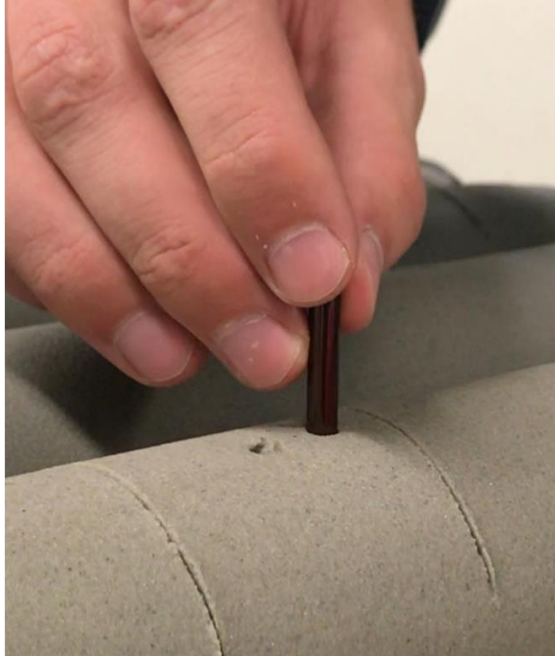


Fig. 9. Micro-CT samples are taken by pushing 3-5mm Kapton® polyimide tubes into the retrieved soil samples from Fig. 8 and lift them.

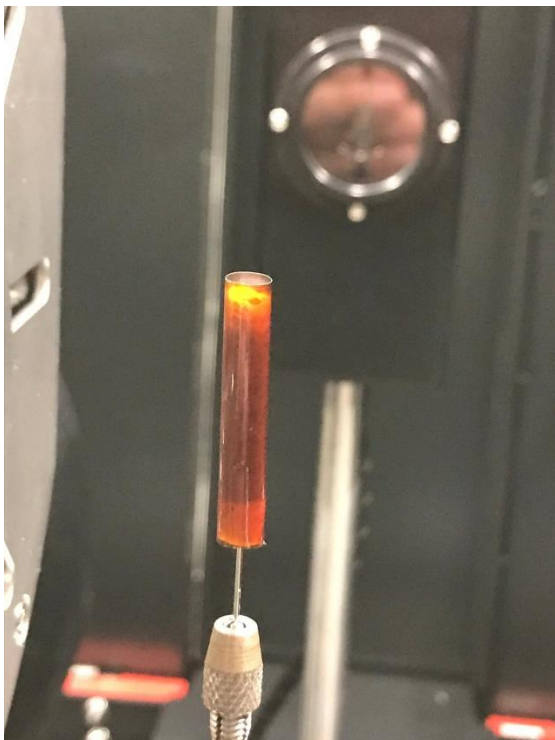


Fig. 10. A prepared micro-CT sample. The sample was lifted out of the retrieved soil sample and tapped with polystyrene foam.

The samples are retrieved by lifting out the carbon straws. Both ends are tapped with polystyrene foam to hold the material in place. For transport a small needle is stitched in one end of the polystyrene foam and stuck on a polystyrene foam board similarly to the sample installation in the CT-scanner (Fig. 10). A total of 6 micro-CT samples has been prepared (Table 2).

Table 2. The depths of the undisturbed samples retrieved expressed in metres below ground level.

Undisturbed samples locations	
S.OG.3	3.82 m-GL
S.OG.6	5.30 m-GL
S.OG.9	6.81 m-GL
S.OG.9A	6.86 m-GL
S.OG.11	7.83 m-GL

2.3. Obtaining absolute K-values

Undisturbed soil samples were used to determine their absolute K -values through a multi-step workflow using micro-CT scans to load the pore space into a PNM. The exact steps are summarized in Fig. 11.

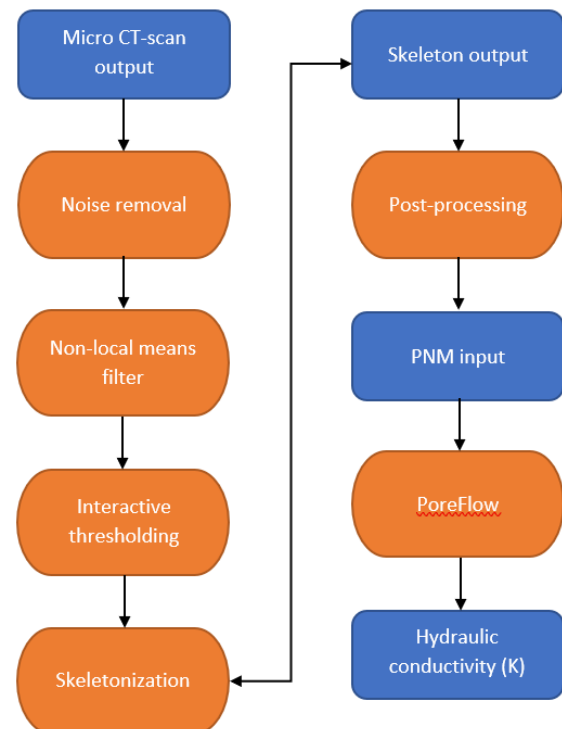


Fig. 11. The workflow to extract absolute K -values from micro-CT scans by using Avizo 9.5 for image segmentation and PoreFlow (Raouf et al., 2013) for pore-network modelling.

2.3.1. Micro-CT scanning

The scans have been made with a Zeiss Xradia 610 Versa. The scanner is based on sample rotation and uses a two-stage magnification architecture to enable sub-micron resolution on large scanning volumes. A photon-converting scintillator that converts the coned-beam x-rays to a visible light image is used and magnified with objective lenses before image acquisition by a CCD (Charge-Coupled Device) detector (White & Kelly, 2020; [Zeiss product information](#)). The imaging field of view (FOV) ranges from tens of micrometres to tens of millimetres while the maximum resolution is 500nm.

For obtaining the best results, an optimum has to be found between the FOV, spatial resolution and beam time. Ideally the imaging FOV equals the REV to gain maximal results with a minimum scanning time. It is the minimum volume where the physics that cause permeability in the sample occur.

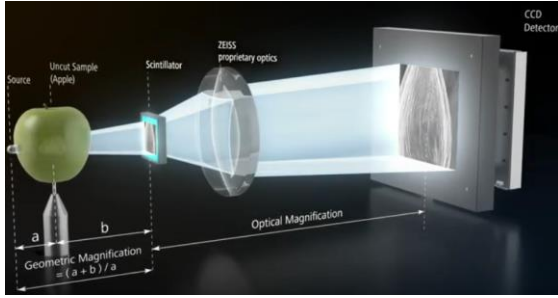


Fig. 12. From [Zeiss microscopy](#). The micro-CT setup where a rotating sample is placed between the x-ray source and scintillator to transform the x-rays to visible light. An optical lens is used for extra magnification before reaching the detector (CCD). a is the Source Object Distance (SOD) and b the Object Detector Distance (ODD). They are variable for tuning the FOV and spatial resolution.

Higher spatial resolutions are achieved by magnifying the sample onto the detector. This can be done by moving the sample closer to the source ([Eq. 11](#); [Fig. 12](#)). But concomitantly, so does the image blurring on the detector (r_s) caused by the spot size of the x-ray source ([Eq. 12](#); Feser et al., 2008).

$$M = \frac{SOD + ODD}{ODD} \quad (11)$$

Where M is the geometric magnification, SOD the Source Object Distance and ODD the Object Detector Distance.

$$r_s = S_x \frac{ODD}{SOD} \quad (12)$$

Where S_x is the spot size of the x-ray source. It is influenced by the current [μA] used to generate the electron, and the source energy [kV] determining the acceleration of the electrons going through the samples (Bartels, 2018).

The theoretical spatial resolution can be expressed as:

$$r_{total} = \sqrt{\frac{r_D^2 + r_s^2}{M}} \quad (13)$$

Where r_{total} is the theoretical spatial resolution and r_D is the resolution of the detector. The voxel size (3D pixel) determining the size of the image often corresponds to the detector pixel size. Hence when the detector size remains the same, the FOV gets smaller when the voxel size gets smaller and vice versa.

Another parameter influencing the spatial resolution is the Signal to Noise Ratio (SNR). The noise has various sources such as the geometrical setting and amplifier. Another source comes from loading images from the CCD. This type of noise can be described as the square root of the signal as it follows a Poisson distribution ([Eq. 14](#); Bartels, 2018):

$$SNR = \frac{Signal}{Noise} = \frac{Signal}{\sqrt{Signal}} \quad (14)$$

This type of noise can be reduced by binning the CCD-pixels before loading. The Zeiss Xradia 610 versa provides the binning 2 option meaning that 2 pixels in both x and y direction are binned into one large pixel. As a result, the signal has increased by a factor of 4 while the noise remains resulting in a reduction of the SNR by a factor 2 without compromising on beam time and FOV:

$$SNR_{binned} = \frac{4*Signal}{Noise} = \frac{4*Signal}{\sqrt{4*Signal}} = 2\frac{Signal}{\sqrt{Signal}} = 2SNR_{unbinned} \quad (15)$$

Other measures to increase the SNR are increasing the beam energy and/or exposure time. However, the effect is limited and it can increase the beam time significantly resulting in higher costs.

Before start scanning, the REV has to be estimated for optimal results. This is done by a

short (2hr) scout scan over a relatively large volume with low resolution.

After the scout scan decisions have to be made regarding the high-resolution scan. As mentioned, it is a delicate balance between sample size, spatial resolution and beam time. The general rule is that the smallest grains comprise of 12-18 voxels to guarantee good characterization of the pore throats. The scanning parameters for all samples are listed in [Table 3](#).

Table 3. The micro-CT metadata of all samples used for further analysis.

Sample	Voltage [kV]	Current [µA]	Exp. Time [sec]	Opt. Mag	Vox size [µm]	SOD [mm]	ODD [mm]	Binned	FOV [mm3]
CT1a	40	75	5	3,98	1,85	28	11	Yes	6,33
CT1b	40	75	45	19,94	0,56	15	11	No	0,16
CT2	40	75	5	3,98	2,01	2,4E-05	-1,0E-05	Yes	17,81
CT3	40	75	6	3,98	2,02	25	11	Yes	8,27

2.3.2. Image processing

After scanning a 3d image is reconstructed based on grey-values representing the attenuated intensity I . Before starting image segmentation, the original reconstructed scan data is first corrected for noise removal by exerting a centre-shift correction and if applicable a beam hardening correction.

The centre shift correction removes artifacts as a result of the sample not being perfectly symmetrically installed. Micro-CT images are being taken while the sample is rotating. If the sample is not perfectly symmetrical, this leads to the sample virtually 'spinning' like a top resulting in irregularities in the reconstructed 3d image. It must be clear that the centre-shift correction is limited meaning that the sample still has to be installed as symmetrical as possible.

The beam hardening corrects for beam hardening artifacts. It is a result of the x-ray beam being polychromatic (photons have different energy and wavelength). For materials the attenuation coefficient decreases when the incoming x-rays are more energetic i.e., "harder" beams have more penetration power according to the Lambert-Beer law:

$$I = I_0 \exp(-\mu x) \quad (16)$$

Where I is the attenuated intensity, I_0 the initial radiation intensity, μ the attenuation coefficient and x the sample thickness.

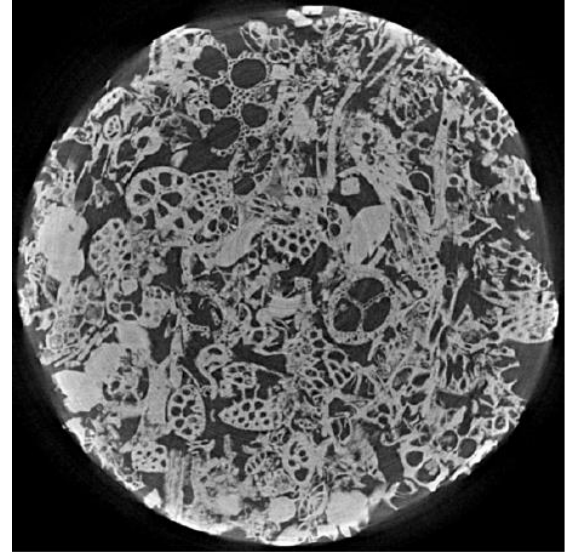


Fig. 13. From Wildenschild & Sheppard, 2013. A micro-CT scan of Mt. Gambier limestone showing beam hardening artifacts such as an apparent increase in attenuation at the edges and streaks between dense objects.

When a polychromatic beam hits the sample, the "softer" x-rays are absorbed quickly leaving only the harder x-rays to penetrate through the sample. This results in an apparent high attenuation coefficient near

the sample edges (Fig. 13). Similar to the centre-shift correction, there is no perfect solution filtering out all beam hardening artifacts. Especially when the sample consists of heterogeneous material since each material hardens beams in different ways (Wildenschild & Sheppard, 2013).

After image correction the scan data is imported into the image processing software Avizo 9.5. A non-local means filter is applied to further remove noise to improve the contrast between pore space and matrix. It works only for removing random noise. Unlike local means filters where the target pixel is smoothed by taking the average value of x surrounding pixels, the non-local means filter uses the average of all pixels in the image weighted by how similar they are to the target pixel. The result is less loss of image detail compared to local means algorithms (Fig. 14; Buades et al., 2005). The algorithm is however computationally intensive increasing quadratic with the number of pixels in the image.



Fig. 14. From Buades et al., 2005. Image denoising through a non-local means filter. Left: original image where gaussian white noise with zero mean and variance is imposed. Right: Denoised image approaching the original image.

Then the image is binarized by imposing an interactive thresholding filter to separate the pore space. Interactive thresholding means to separate the image grey-value distribution into an image that consists of just two grey-values i.e., a binarized image. The threshold grey-value is manually defined at the pore-matrix interface resulting in an image where the pore space is segmented from the matrix.

The segmented pore space has to be exported from Avizo such that it can be used as an input for the PNM. For this, the auto-

skeleton module is used. It transforms the segmented pore space into a pore-network skeleton equidistant to the matrix shape boundaries (Fig. 15). At every kink in the skeleton (points) the pore diameter is given.

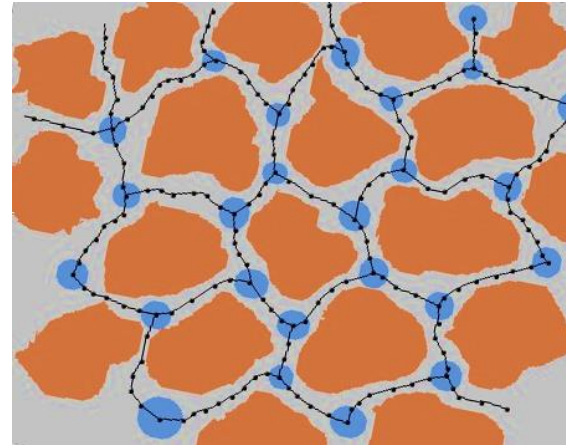


Fig. 15. A schematic drawing of the auto-skeleton output in Avizo 9.5. The blue spheres represent the pore bodies (nodes), the black dots at the kinks of the skeleton structure are the points providing the local pore diameter. The black lines connecting the nodes are the segments.

2.3.3. Generate input files pore-network-model (PNM)

After skeletonization in Avizo the pore structure is defined in terms of nodes (pore bodies) linked by segments (pore throats) represented a series of pore points located at the kinks providing the local pore diameter (Fig. 15; Fig. 17). The idea is to simplify the pore structure into spherical pore bodies interlinked through cylindrical pore throats compatible with a PNM (Fig. 16).

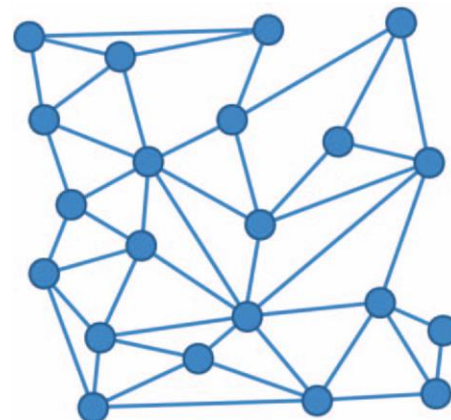


Fig. 16. From Joekar-Niasar & Hassanizadeh, 2012. A schematic drawing of an unstructured irregular pore network.

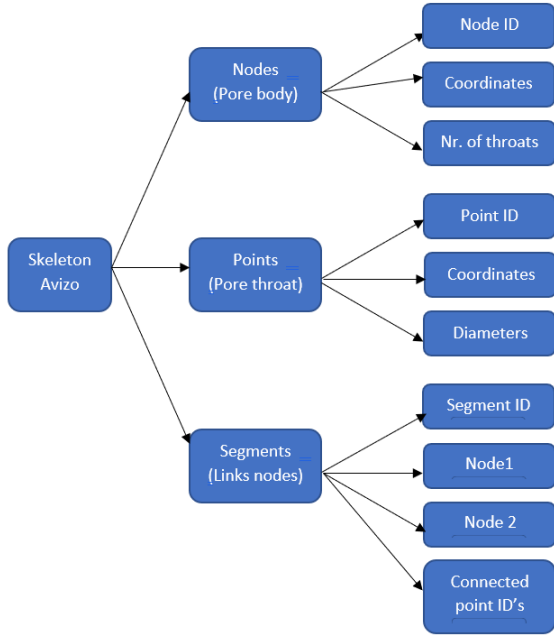


Fig. 17. An overview of the skeleton data structure. The node data describes the pore bodies where the pore throats link. The point data represents the locations where the skeleton structure has kinks (Including nodes). The segment data explicitly links the nodes to each other and provides the points involved along the pathway.

The cylindrical throat is characterized by a throat length (L_{throat}), and throat radius. The throat length is set to be the sum of Euclidian distances between the points along the pore segment (Eq. 17):

$$L_{throat} = \sum_{PointNodeID1[j]}^{PointNodeID2[j]-1} d_{Pj,Pj+1}(x,y,z) \quad (17)$$

Where d is the Euclidean distance between two points along the pore segment.

The throat radius is determined by taking the harmonic mean of all point radii along the same segment is taken since the bottleneck effect causes the representative permeability of the pore throats to tend to the lower point diameters (Godoy et al., 2019).

Additionally, the tortuosity of the simplified pore throats can be calculated by dividing the calculated pore length by the Euclidian distance between the nodes (Eq. 18):

$$\tau = \frac{L_{pore}}{d_{n1,n2}} \quad (18)$$

The spherical pore bodies are determined by the point radius at the corresponding location.

2.3.4. Generation of PNM and programs used

As mentioned in the introduction, the choice for a PNM to determine K is based on the computational efficiency with respect to direct fluid flow models, and the expertise on PN-modelling in the hydrogeology group at Utrecht University. Nevertheless, direct fluid flow models are already the standard for single-phase flow- and transport (Blunt et al., 2013). For multiphase flow PNM show currently better results compared to direct fluid flow methods (Blunt, 2001; Blunt et al., 2013; Bultreys et al., 2016). PNM's are a simplification of the pore space meant to capture all relevant topological attributes of the porous system. It is expected that direct fluid flow models will be favoured in the future due to rapid improvements on computation efficiency as these methods better approach reality.

For pore-network modelling the in-house PNM PoreFlow is used (Raof et al., 2013). In this study we are interested in modelling uniform single-phase flow only as a simple application. The flow field is generated by imposing a pressure difference over the PNM where the boundaries parallel to the flow direction are treated as no-flow boundaries. Flow through the cylindrical pore throats is assumed to approach the Hagen-Poiseuille equation:

$$q_{th} = \frac{\pi r_{th}^4 \Delta P_{th}}{8 \mu L_{th}} \quad (18)$$

Where q_{th} is the total volumetric flow rate through a cylindrical pore throat. r_{th} the throat radius. ΔP_{th} is the pressure difference over the pore throat, μ the fluid viscosity and L_{th} the throat length.

The average flow velocity through the network can be described as:

$$\bar{v} = \frac{Q_{tot} L}{V_f} \quad (19)$$

Where L is the total network length, V_f the total fluid volume and Q_{tot} is the total volumetric flow rate which is the sum of the difference in flow-rate between all throat inlets and outlets:

$$Q_{tot} = \sum_{k=1}^{N_{throats}} (q_{k,in} - q_{k,out}) \quad (20)$$

The permeability is calculated as followed:

$$k = \frac{\mu Q_{tot} L}{A \Delta P} \quad (21)$$

Where k is the permeability, A the cross-section of the network and ΔP the total pressure difference applied.

Finally, the permeability can be converted to K through the following formula:

$$K = \frac{k \rho g}{\mu} \quad (22)$$

Where ρ is the fluid density and g the gravitational acceleration.

For each sample the flow is simulated in vertical direction corresponding to the horizontal flow direction during HPT-profiling. A constant flux boundary condition is set to an average pore velocity through the porous medium of 1e-5 m/s (Table 4).

Table 4. The input parameters for the pore-network-model (PNM). The boundary condition (B.C) is a constant flux meaning that the pressure gradient is adapted such that the average pore velocity matches the input value.

PNM input parameters	
Flow type	Single-phase
Fluid viscosity	0.001 Pa*s
Fluid density	1000 Kg/m ³
Flow B.C	Constant flux
Pore inlet	100 Pa
Pore velocity	1E-5 m/day

2.4. HPT-calibration

The HPT-profiles are calibrated to the absolute K -values determined through micro-CT scans and PN-modelling. The data is plotted along the Q/P_{corr} profile. Then the mean average error (Eq. 23) of the Q/P_{corr} profile at the

depths of absolute K -values with $\pm 0.1m$ uncertainty is taken as the translation constant.

$$MAE = \frac{1}{n} \sum_{i=depth(k)-0.1}^{depth(k)+0.1} |k_i - k| \quad (23)$$

Where k_i are the points along the Q/P_{corr} profile and k the absolute K -value from PN-modelling. When data after translation becomes negative, it is assigned a value of 1E-3. The same procedure is applied for the K -models described by McCall & Christy, 2010 and Borden et al., 2020.

After calibration the HPT-profiles are compared to discrete interval slug tests along the profile. The heterogeneity in K is assumed to be represented by horizontal layering parallel to the HPT-flow at the HPT length-scale (cm). Hence the average K can be calculated by taking the arithmetic mean of the HPT-profile (Freezer & Cherry, 1979). The arithmetic mean of the HPT-profiles is taken along the depth intervals of the slug tests and compared to the K -values obtained from the slug tests.

3. Results

3.1. HPT profile

A total of 3 HPT-profiles were made of whom HPT1 is situated close ($\pm 1m$) to the borings where the calibration data and lithology are obtained (Fig. 1). Hence the focus is on HPT1 with the empirical K -models from McCall & Christy, 2010 and Borden et al., 2020 which are all plotted in Fig. 18 along the corresponding lithology. HPT-measurements were taken at a 1.5cm interval while the probe advancing rate yielded 2cm/s. Assuming that Q/P_{corr} is a proxy for K based on Darcy's Law (Eq. 2), it shows little correlation with the interpreted lithology. It is expected that Q/P_{corr} increases with sand fraction. This does not happen. The sandy layers show K -values (0.2 – 6 m/day) that can be expected from fine sands while the silty-clayey layers show K -values a few orders of magnitudes higher as expected (Bear, 1972).

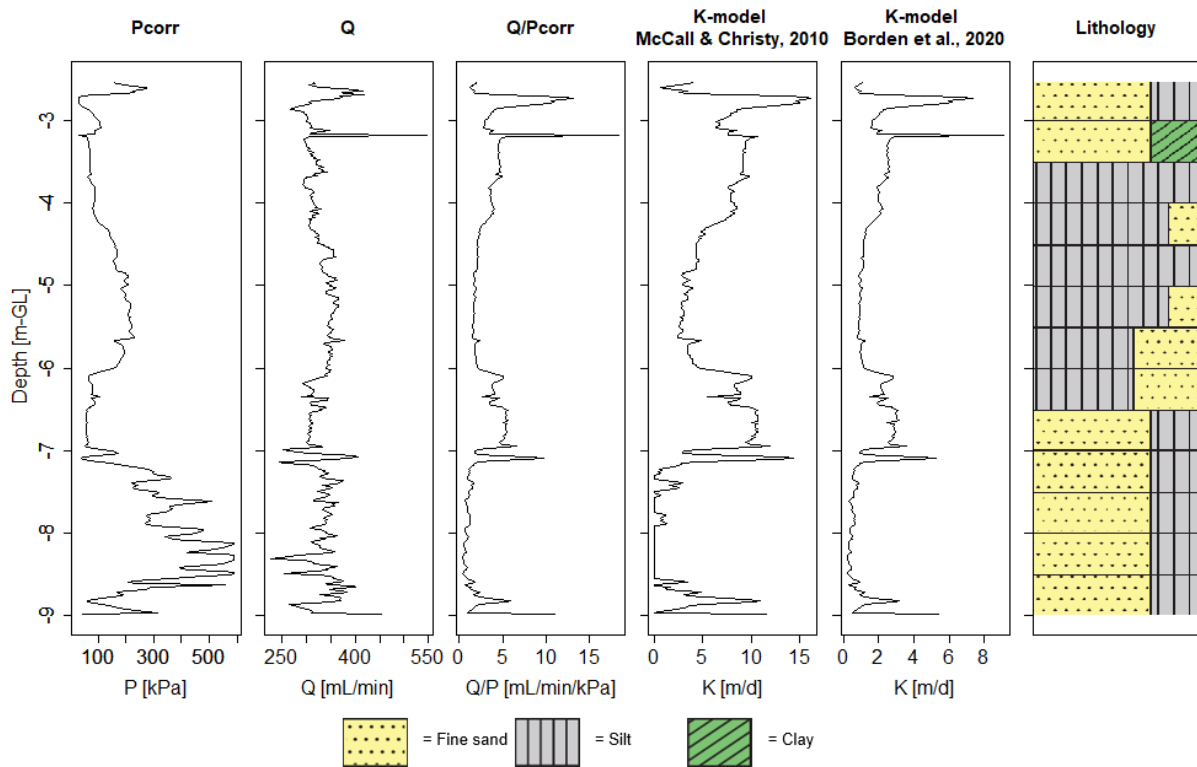


Fig. 18. HPT1-profile measured in Son, The Netherlands at a depth between -2.5m-GL (depth below Ground-Level), and -9.0m-GL (A+B). The Q/P_{corr} as a proxy for K (C), the built-in K -model from the [GeoProbe software](#) (D) with the results of the K -model postulated by Borden et al., [2020](#) (E), and the lithology distribution along the profile acquired 1m from the HPT-well (F).

3.2. Geostatistical analysis

Multiscale vertical correlation lengths have been determined for the HPT1- Q/P_{corr} dataset by trend decomposition and perform variogram fitting on the obtained subseries with varying length scales.

Variogram fitting demands the data to be stationary (Lapidath, [2017](#)). If not, the data can be transformed to a normal distribution to secure stationarity. A Q-Q plot can be made to check if the data is normally distributed by plotting the empirical data quantiles to the theoretical quantiles of a normal distribution. When normally distributed, the Q-Q plot shows a linear relationship which can be observed in [Fig. 19](#) indicating that log-transformation suffices for this data to secure stationarity.

After log-transformation, the data is decomposed in R analogous to seasonal trend decomposition based on Loess (STL) in timeseries analysis (Cleveland et al., [1990](#)).

The periodic trend decomposition is demonstrated in [Fig. 20](#) where the data is unravelled in a small periodic component, an intermediate-scale and a small-scale component.

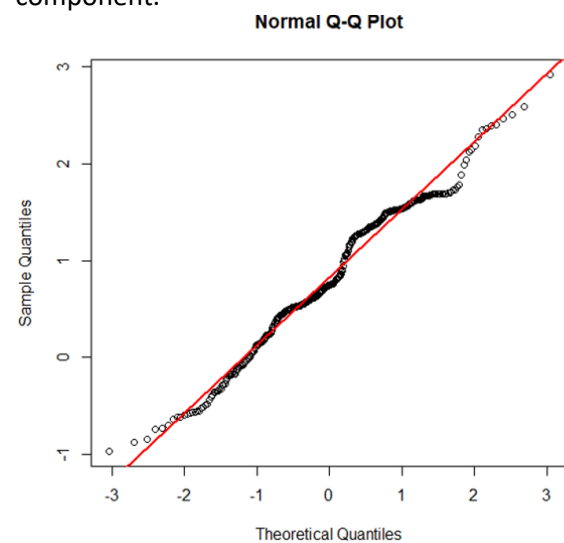


Fig. 19. A Q-Q plot of the HPT- Q/P_{corr} data. The linear relationship between the empirical data quantiles and theoretical quantiles show that the data is normally distributed.

Variogram fitting has been performed on both small- and intermediate scale (Fig. 21) where the effective range corresponds to the correlation length λ . The variogram fitting and the calculated correlation lengths are summarized in Table 5.

Table 5. The correlation lengths for the intermediate- and small scale obtained through variogram fitting (Pebesma, 2004).

	Scale	Correlation length (m)	Variogram model
λ_1	Intermediate	1.69	Wave
λ_2	Small	0.21	Exponential

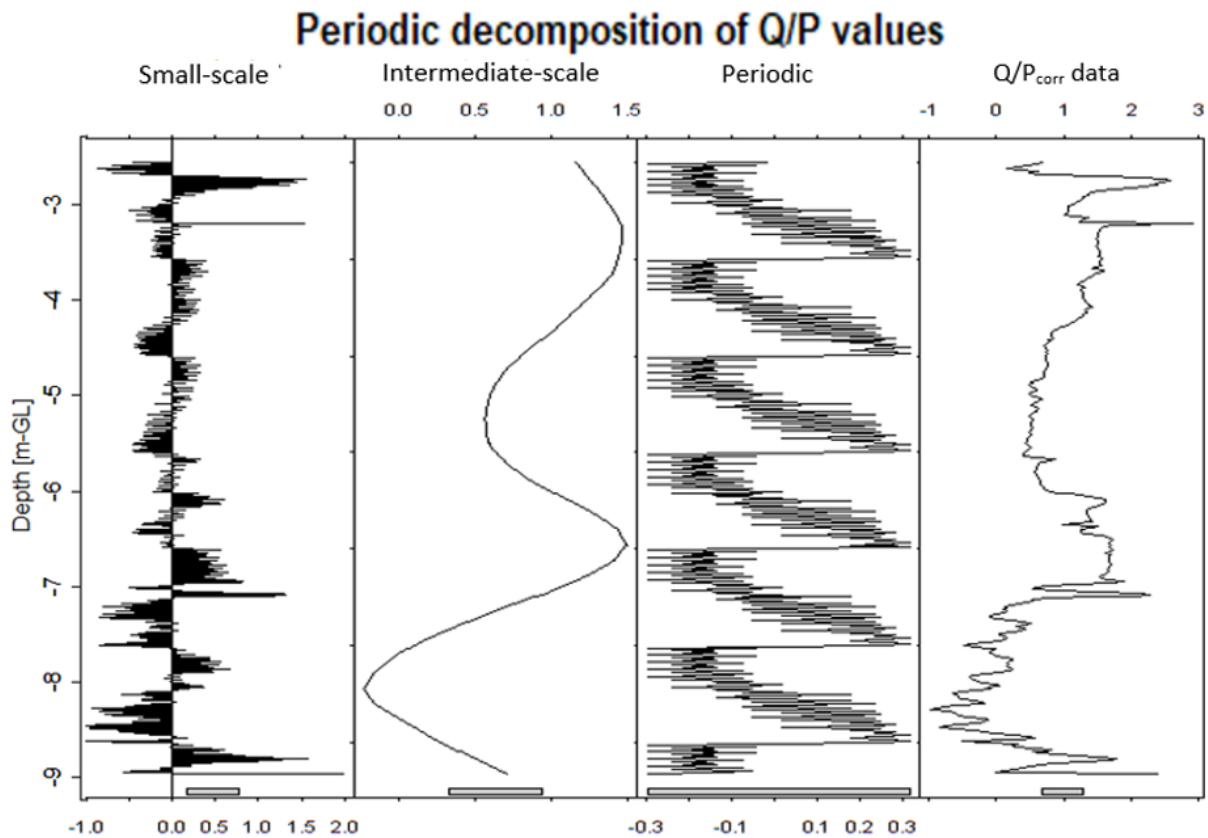


Fig. 20. The periodic trend decomposition of $\text{Log}(Q/P_{\text{corr}})$ as described in Cleveland et al., 1990. The data column shows the original data (right). Then a periodic component is subtracted (mid-right). Subsequently a moving average is taken as the trend describing the intermediate-scale variations (mid-left). After removing the trend, the remainder is left describing the small-scale variations (left).

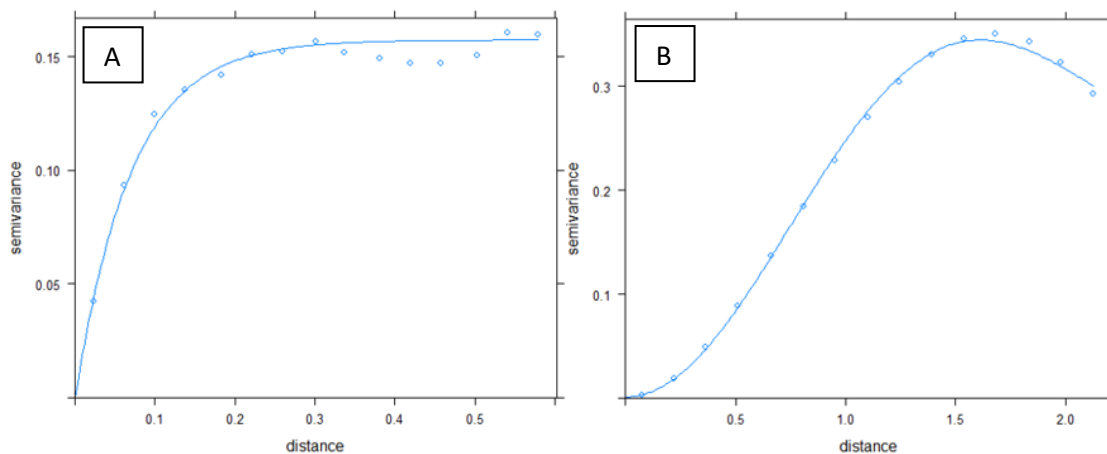


Fig. 21. Variogram fitting by using an exponential ACF for the small-scale (A), and a Hole effect (wave) ACF for the intermediate-scale data series.

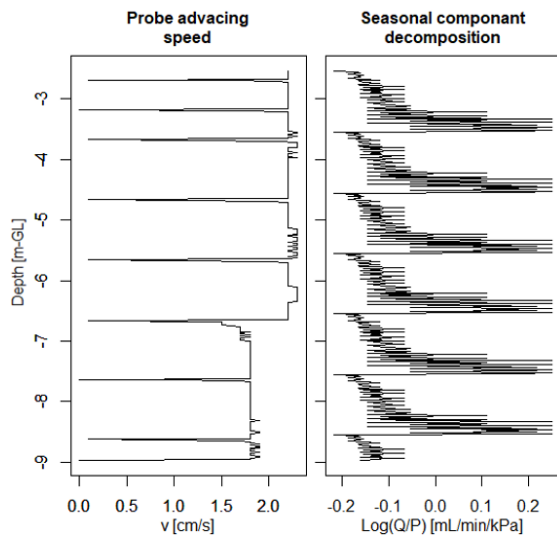


Fig. 22. Strong correlation between the probe advancing speed (left), and the decomposed periodic subseries (right; Fig. 20).

An interesting correlation between the probe advancing speed (V) and the decomposed periodic subseries can be observed (Fig. 22). Through the periodic component, the impact of the periodic setback of the probe advancing speed on the Q/P_{corr} data can be estimated. The variability of Q/P_{corr} to V can be estimated by twice the amplitude of the periodic subseries which is around 0.61 [ml/min/kPa].

3.3. Waterglass

To test the suitability of waterglass in combination with micro-CT scanning, 4 different mixtures have been prepared and added to dry sand to test the contrast between matrix and pore space (Table 1). The results show that for all mixtures this contrast is visible (Fig. 23).

The field experiment however failed. The waterglass was injected, but not as effective as planned. Normally one installs the system and leaves it for two days to let the soil above the injection point compact to hold back the waterglass when injected at depth. Due to circumstances this time was shortened with the result that the waterglass followed the road of less resistance, which was up. The waterglass could not be injected at a lower rate, because it was already gelatinizing.

The sand where waterglass was present, did not break at the bottom during sampling making the sample tube come up empty. When

the sample is pulsed at depth, the sand breaks off and is successfully retrieved.

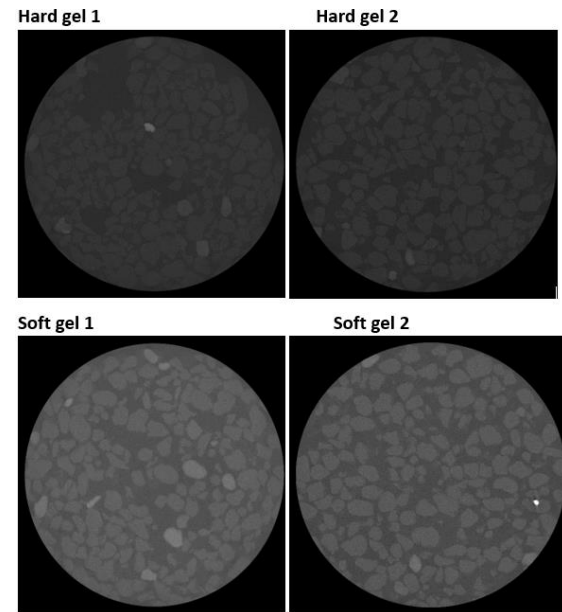


Fig. 23. The waterglass mixtures with dry sand from Table 1. All mixtures show contrast with the matrix.

3.4. Micro-CT images + segmentation

A total of 5 samples have been retrieved and prepared for micro-CT scanning. The samples with corresponding depths are listed in Table 6. Samples CT2 and CT4 appeared to be disturbed while doing the scout scan. The rest was successfully retrieved and prepared.

Table 6. The prepared micro-CT samples with corresponding depths in the field expressed in metres below ground level. The successfully retrieved and prepared samples are marked grey.

Samples for micro-CT scanning		
CT1	3.82 m-GL	Undisturbed
CT2	5.30 m-GL	Disturbed
CT3	6.81 m-GL	Undisturbed
CT4	6.86 m-GL	Disturbed
CT5	7.83 m-GL	Undisturbed

The scans with corresponding segmentation are listed in Fig. 24. Segmentation proved to be difficult for sample CT1 when the grain size drops below $10\mu\text{m}$. For good pore geometry characterisation, the pore throat ideally consists at least 10-12 voxels. The problem is that a very high spatial resolution is required. This can either be done by increasing the beam

time significantly (costly), or by unbinning the detector voxels resulting in a reduction of the Signal to Noise Ratio (SNR) by a factor of 2 (Eq. 15). The result is that either the spatial resolution is sufficient with $0.56\mu\text{m}$, but the noise becomes too dominant creating fake throats and making segmentation very hard (CT1A). Or that the noise is controllable but the spatial resolution is not sufficient with $1.85\mu\text{m}$ (CT1B).

Samples CT3 and CT5 were easier to analyse with a voxel size of $2.02\mu\text{m}$. Note that the grain size distribution of CT3 is very heterogenous making the material dual porous and harder to model fluid flow (Šimunek & van Genuchten, 2008; de Vries et al., 2017). Sample CT5 is well segmented and homogeneous making it ideal for determining its permeability.

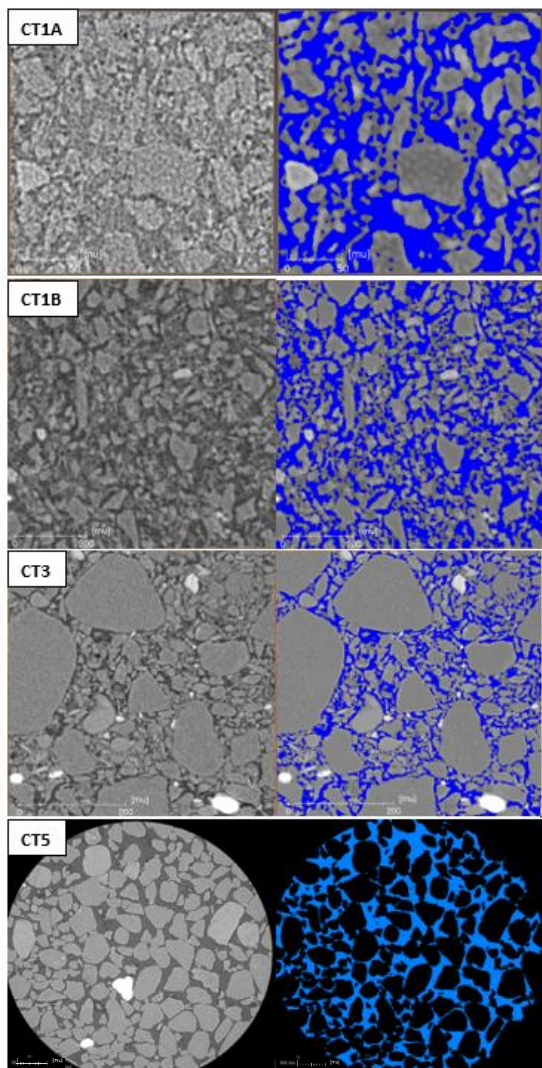


Fig. 24. Micro-CT scans for all undisturbed micro-CT samples. Sample CT1 was segmented using the different voxel sizes of $0.56\mu\text{m}$ (CT1A), and $1.85\mu\text{m}$ (CT1B). Samples CT3 and CT5 were scanned with a $2.02\mu\text{m}$ voxel size.

3.5. Pore network analysis

Fig. 25 shows a typical input of a pore-network model (PNM) obtained from sample CT5. The absolute tube radii are plotted instead of a representation as is often done.

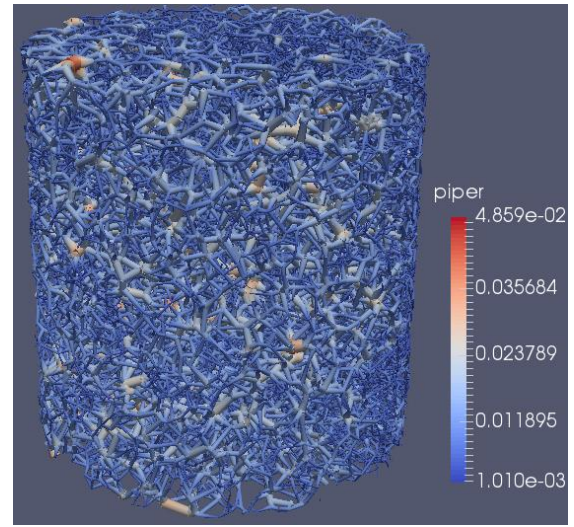


Fig. 25. A visualisation of the CT5 pore-network model extracted from Avizo. The throat radii are expressed in μm .

A summary of the pore statistics of each sample is listed in Table 7. All samples show a positively skewed distribution indicating a log-normal distribution. Note the very high skewness and low variance in CT1B and CT3 indicating that most of the pores throat radii are represented by the minimum voxel size. Table 7. A summary of pore throat statistics of each sample after segmentation by using the harmonic average of the throat points (Godoy et al., 2019). The parameters are expressed in μm .

Throat radii statistics				
[μm]	CT1A	CT1B	CT3	CT5
No. throats	29.338	116.174	155.326	75.072
Mean	1.54	1.07	1.06	8.43
Min	0.28	0.92	1.01	1.01
Max	6.31	11.20	5.31	49.54
Variance	0.69	0.16	0.04	34.26
Median	1.37	0.92	1.01	7.12
Skewness	1.09	5.55	6.89	1.16
Kurtosis	4.18	49.88	65.02	4.56
Max/Min	22.67	12.11	5.26	49.07

The final K -values obtained through PN-modelling are itemized in [Table 8](#). The results indicate that the difference between arithmetic, geometric and harmonic averaging is rather small ($\pm 30\%$). Samples A and B of CT1 show one order of magnitude difference. This can be linked to the coarse resolution in CT1B where small errors in segmentation have large effects on the outcome of K . In this case an underestimation.

Table 8. Hydraulic conductivities (K) obtained through PN-modelling from samples taken at B03.

Sample	Resolution [μm]	K arithmetic [m/d]	K geometric [m/d]	K harmonic [m/d]
CT1A	0.56	1.39E-02	1.15E-02	9.44E-03
CT1B	1.85	1.26E-03	1.07E-03	9.35E-04
CT3	2.01	1.30E-03	1.21E-03	1.14E-03
CT5	2.02	3.38E-01	2.77E-01	2.26E-01

3.6. HPT calibration

All HPT profiles were calibrated to CT5 ([Fig. 26-27](#)), the most reliable absolute K -value determined with the PNM since it is the only homogeneous sample that shows good segmentation. The results were compared to 4 slug tests performed in the vicinity of HPT1 ([Fig. 1](#); [Table 9](#)). The depths of the slug tests for

comparison are set to the depth of the gravel layer. Subsurface heterogeneity seems to affect the outcome of the different HPT profiles.

The K -values obtained with the PNM and slug test confirm the hypothesis that low conductivities are expected when the material consists of more clay and silt. Paradoxically the HPT1-profile indicates the opposite in the upper 3-4m showing higher Q/P_{corr} values in the silty layers compared to the sandier layers further down the profile at -7.5m. These sandy layers show better fits to slug test 3 and 4 ([Fig. 26-27](#)). Especially the calibrated Borden solution with slug test 3. Despite being partly out of range the profile has potential to fit slug test 4 given that further down no undisturbed could be taken due to the material being too coarse.

Table 9. Locations and K -values from the slug tests performed at HPT1 (Slug 1+3), and where undisturbed samples were taken (Slug 2+4).

	Depth min [m-GL]	Depth max [m-GL]	Depth min gravel [m-GL]	Depth max gravel [m-GL]	K [m/d]
Slug1	3.5	4.5	3.0	5.0	5.00E-02
Slug2	6.3	6.4	6.0	6.5	1.80E-01
Slug3	7.0	8.0	6.5	8.5	8.80E-01
Slug4	8.9	9.1	8.9	9.4	4.58E+00

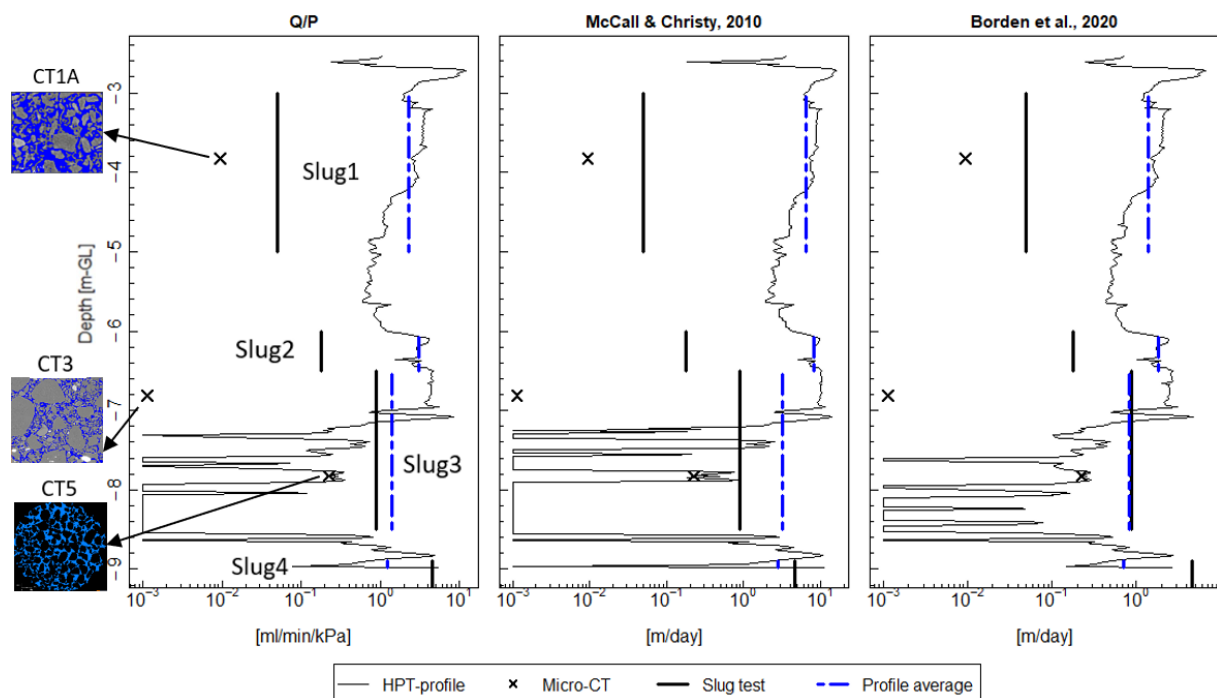


Fig. 26. HPT1-profile with log-scale calibrated to CT5 with the results of the micro-CT/PNM and slug tests. The CT-scans and small slug tests (2 and 4) have been obtained 1m from HPT1 while slug tests 1 and 3 have been obtained at HPT ([Fig. 1](#)).

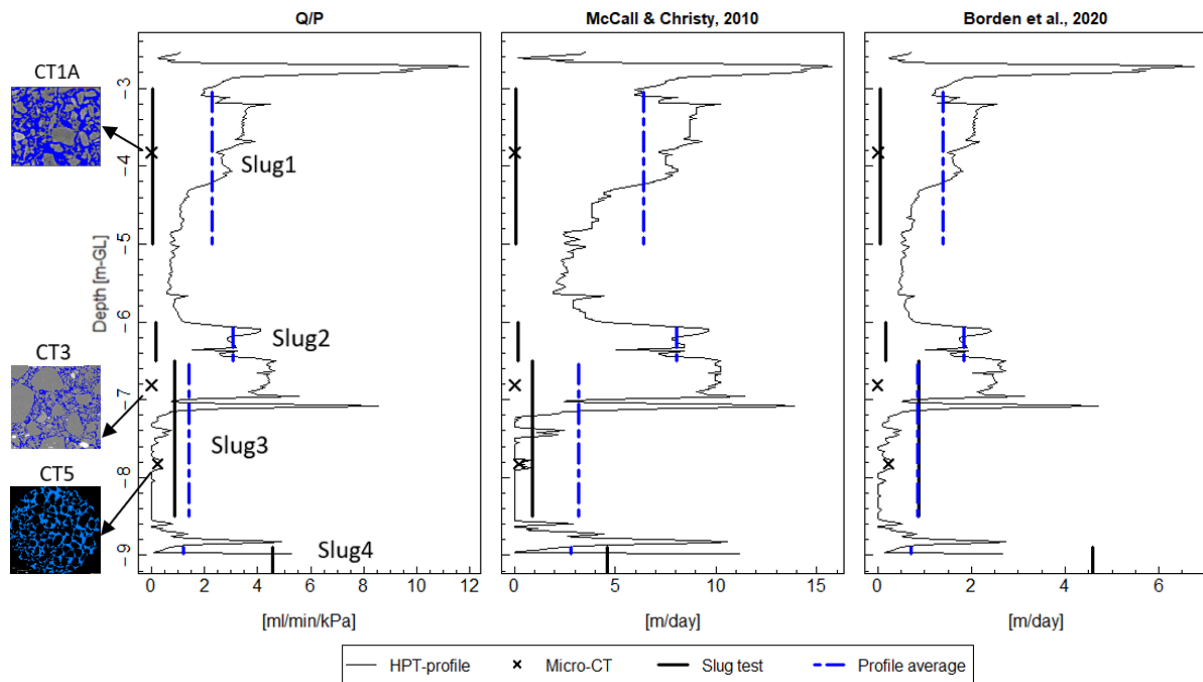


Fig. 27. HPT1-profile with linear scale calibrated to CT5 with the results of the micro-CT/PNM and slug tests. The CT-scans and small slug tests (2 and 4) have been obtained 1m from HPT1 while slug tests 1 and 3 have been obtained at HPT (Fig. 1).

4. Discussion

4.1. Reliability of the HPT measurements

The calibration of the HPT-profiles through pore-network modelling shows potential to work when it is coupled to the empirical model from Borden et al., 2020. It is seen in Fig. 26-27 where the profile is calibrated to sample CT5 retrieved at a 1m distance from the profile and matches very well with slug test 3. It is however the only depth where a good match is observed. A second good fit is possible at the deepest slug test 4 where HPT1 does not cover the entire depth range of the slug test. Although slug test 4 outranges the HPT1-profile, a good fit is realistic given the profile trend and the deeper higher conducting layers where no undisturbed samples could be taken.

Noticeable is the mismatch between the upper 4m of the HPT1-profile and the absolute K -values obtained from both the slug tests and PN-modelling are 1-2 orders of magnitude. It is probably the result of redundant measurements for being at the upper measurable range of the pressure. This effect

seems to happen for $K < 0.1\text{m/day}$ (Fig. 27). The mismatch of CT3 can be explained by its dual porous nature. Due to time constraints, only a small volume could be scanned where the small-scale porous features are visible. Hence the sample is biased towards the small grain fraction leading to underestimation of K .

To interpret the results, it is essential to realise that all three techniques to obtain K measure at different length scales (Table 10). This inherently means they capture different aquifer features when the aquifer is not strictly homogeneous.

Hence the discussion that water may flow alternative paths of less resistance such as cracks or a highly permeable adjacent layer, which are features that the micro-CT sample does not capture, is false since the slug test would cover these features and show similar K results to the HPT-profile.

Table 10. All measurement techniques used in this study to determine K and their corresponding length scales.

	Length scale
Micro-CT	mm
HPT	cm
Slug test	dm/m

A better explanation can be found in a scatterplot of 74 paired HPT-slug tests from locations throughout the Midwest, USA (McCall & Christy) and 68 from The Netherlands (Fig. 28). The dataset reveals that the paired slug test shows a 1-2 order of magnitude difference in K for the same average Q/P_{corr} . This means that no unequivocal relationship exists between Q/P_{corr} and K . The relationship also seems rather linear instead of exponential as proposed by McCall & Christy, 2010.

Explanations for the spread in K -values for the same Q/P_{corr} are horizontal anisotropy and subsurface heterogeneity. The HPT only

measures Q/P_{corr} in only a single direction. When the HPT-flow is not in direction of the paired slug test, horizontal anisotropy due to non-isotropic sediment bedding structures, can cause K to variate for the same Q/P_{corr} . The same applies for subsurface heterogeneity where the lithology changes at a typical distance of 1m between the HPT-profile and slug test.

In Fig. 29 the Borden solution (Eq. 4) is compared to the results from 68 slug tests along HPT-profiles throughout The Netherlands. The plot shows a 1:1 relationship when the Borden solution is multiplied by a factor of 2 meaning that E now equals 1.232 for the Dutch situation. It can also be observed that the majority of data points fits within the 1 order of magnitude range. These findings show that the Borden solution performs better in predicting slug tests for the Dutch subsurface when multiplied by a factor of 2.

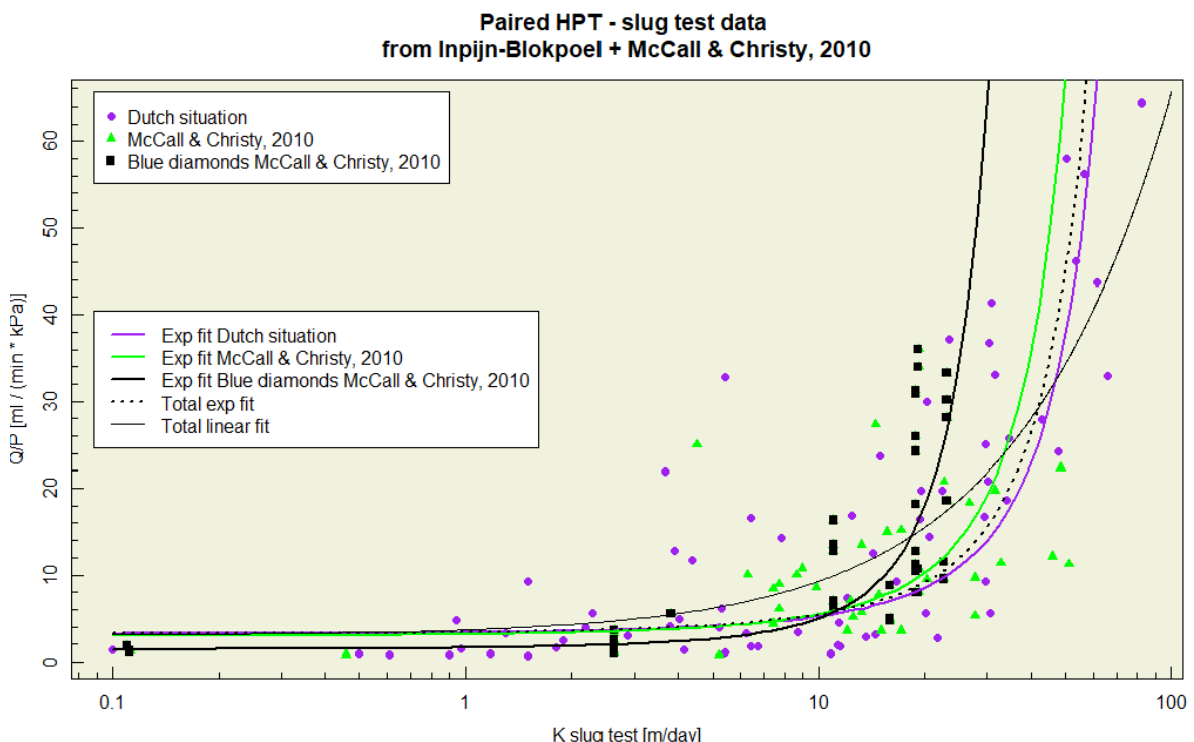


Fig. 28. Paired HPT-slug test data from McCall & Christy, 2010 (Fig. 2) and the Dutch situation measured throughout The Netherlands. Note that for the total data the linear fit performs best.

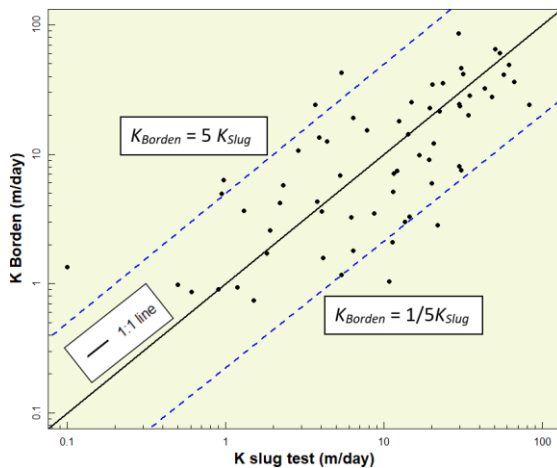


Fig. 29. K predicted using Eq. 4 from Borden et al., 2020 versus the measured K from slug tests.

It is important to realise that slug tests cannot be treated as the absolute truth. Although they are assumed to be in this research. It is suggested that slug tests tend to overestimate K as the higher conducting layers are overly dominant (Bouwer, 1989; Hyder & Butler, 1995). This is however rebutted by Son & Koch, 2014 claiming that slug tests rather underestimate K except for low conductivity values ($K < 1\text{m/day}$).

4.2. Geostatistical analysis

The geostatistical analysis shows that HPT-profiles can successfully be decomposed to obtain vertical correlation lengths on multiple length scales. The data is ergodic and stationary meaning that the dataset has a constant mean and that it is large enough to capture all statistical properties which do not change when the dataset becomes larger. When the dataset is not stationary it must be transformed to a gaussian distribution. In this case a log-transformation is sufficient.

4.3. Retrieving undisturbed samples

Taking undisturbed samples proved being difficult when the material becomes coarse. Hence only fine samples were taken. Even when successfully retrieved from the subsurface, it goes through multiple steps where the material becomes slightly disturbed and compressed. Sometimes resulting in micro-CT samples that are too disturbed (Table

6). This starts with retrieving the samples from the subsurface where frictional drag forces compress the material when the sample tubes are pushed into the ground. The material is further compressed when it is pushed out of the tube into a half-open PVC pipe and at last when an x-ray transparent carbon straw is pushed into the material. Although these compressions are relatively small, they result in a slight underestimation of K .

Disturbance will always be present along the process of micro-CT preparation. What can be improved greatly is retrieving samples from the subsurface. To retrieve coarse materials, it is recommended to experiment with the “gel”-push technique described in Taylor et al., 2012 and Umehara et al., 2015.

4.4. Potential of waterglass

Another solution for both retrieving coarse samples and compression can be found in waterglass. The scans in Fig. 23 show that micro-CT scanning and waterglass can be a fruitful combination. The cohesive effect on retrieving undisturbed samples from the subsurface is still unknown and has to be investigated. The experiment described in section 3.3 failed due to time limitations and should definitely be carried out again to see if retrieving coarse sediments with waterglass is possible.

4.5. Micro-CT scanning

As can be seen in Fig. 24 the quality of the scans and therefore segmentation varies greatly. Sample CT5 shows high image quality and homogeneity while the quality of the CT1 samples is visibly lower. The main reason for the lower quality is the trade-off that had to be made between beam time and image quality. Since the grain size is much lower in CT3 the voxel size had to be significantly lower as well. However, unbinning the detector pixels for CT1A decreased the Signal-to-Noise Ratio (SNR) by a factor of 2 meaning that the relative portion of noise in the scan doubled (Bartels, 2018).

A second major difference between the samples is the homogeneity of the grain size distribution. Samples CT1 and CT5 are relatively homogeneous while CT3 shows a double porosity distribution. When the grain size distribution is homogeneous the REV becomes relatively small. Yet the REV increases when the grain size distribution becomes heterogeneous as in (CT). These samples are not ideal with the current workflow since they need both a high resolution and large scanning volume that generates a lot of data which the PNM cannot handle. Hence dual porosity layers should be avoided when possible for HPT-calibration since they do not provide additional value while being tedious to work with.

4.6. Modelling fluid flow

A PNM is used to determine permeabilities from the micro-CT scans. They require simplified pore geometry inputs. In this case a network of spherical pore bodies connected through cylindrical pore throats. There are other more sophisticated yet complicated techniques available such as OpenFoam®, GeoDict (Math2Market) and Lattice-Boltzmann simulations that are able to simulate water flow through the real segmented volume extracted from AVIZO that could lead to more precise estimates of K . These methods are more expensive and require much more computer power to solve the problem. The main advantage to opt for the in-house PNM called PoreFlow is the expertise in the geohydrology group at Utrecht University and the ability to run fast simulations on a mediocre laptop.

4.7. Calibration strategy

For the calibration strategy the simplest form was chosen to calibrate the entire HPT-profile to a single absolute K -value obtained through PN-modelling by taking the Mean Average Error (MAE) as the translation constant. This was done since only one calibration point (CT5) was interpreted to be reliable enough for calibration. When multiple calibration points

are available along the profile, an arithmetic average of all MAE's should be taken as a common translation constant.

When different sections of the HPT-profile need a different calibration, conditional simulation can be used. Advantage is that no concession is made between calibration points compared to when an average translation constant is taken. The main disadvantage would be the loss of data between the calibration points since they are statistically interpolated through an ergodic random function.

5. Conclusion

The HPT calibration procedure using an upscaling workflow from pore-scale to field-scale through micro-CT scanning and PN-modelling shows potential to work when coupled to the Borden solution. Currently the bottleneck in proving the concept lies at cost-effectively retrieving undisturbed coarse soil samples from the subsurface.

In clayey and silty soils with $K < 0.1\text{m/day}$ the HPT seems to give false results due to the pressure sensor reaching the upper measurable range leading to a narrowed sensitivity and a lot of noise.

For Micro-CT scanning it is recommended to bin the detector pixels and to stick to homogeneous materials with a minimum grain size of at least $20\mu\text{m}$.

To model fluid flow through the segmented porous media a PNM seems to do well. For more complex geometries one can turn to Lattice-Boltzmann simulations or software packages such as OpenFoam® and GeoDict (Math2Market).

5.1. Further research

Currently the inability to retrieve coarse undisturbed soil samples is impeding the HPT-calibration to be complete. For now, “gel-push” techniques prove to successfully retrieve undisturbed sand samples from the subsurface and are definitely an option. Another viable option could be waterglass. The combination of waterglass and micro-CT

scanning has proven to be fruitful. Now the practicability in the field has to be assessed. It is recommended to choose a coarse sandy layer for waterglass injection and wait a few days to let it gelatinize before retrieving an undisturbed sample.

To reduce the effect of horizontal anisotropy and/or subsurface heterogeneity, the HPT-screen should be pointed towards the paired slug tests.

6. Acknowledgements

This project was funded by Inpijn-Blokpoel Ingenieurs and the waterboards HDSR (Hoogheemraadschap de Stichtse Rijnlanden), and WBD (Waterschap Brabantse Delta). I would like to thank my 1st supervisor dr. Alraune Zech, 2nd supervisor Msc. Marloes van Lipzig and external advisor dr. Willem-Bart Bartels for guiding this project and offering me this opportunity to work on such an interesting subject. Your aid was very much appreciated. The micro-CT scans were made with help from dr. Markus Ohl and dr. Oliver Plümper from the Structural geology & EM group, UU and advise from dr. Tom Bultreys, Ghent University. Also special thanks to Enno de Vries for helping me out during the segmentation-to-PNM process.

7. References

- Bartels, W. (2018). *Pore scale processes in mixed-wet systems with application to low salinity waterflooding* (Doctoral dissertation, UU Dept. of Earth Sciences).
- Bear, J. (1972). *Dynamics of Fluids in Porous Media*. Dover Publications. ISBN 0-486-65675-6.
- Blunt, M.J., 2001. Flow in porous media — pore-network models and multiphase flow. *Curr. Opin. Colloid Interface Sci.* 6, 197–207.
- Blunt, M.J., Bijeljic, B., Dong, H., Gharbi, O., Iglauer, S., Mostaghimi, P., Paluszny, A., Pentland, C., 2013. Pore-scale imaging and modelling. *Adv. Water Resour.* 51, 197–216.
- Bohling, G. C., Liu, G., Knobbe, S. J., Reboulet, E. C., Hyndman, D. W., Dietrich, P., & Butler Jr, J. J. (2012). Geostatistical analysis of centimeter-scale hydraulic conductivity variations at the MADE site. *Water Resources Research*, 48.
- Boggs, J. M., Young, S. C., Beard, L. M., Gelhar, L. W., Rehfeldt, K. R., & Adams, E. E. (1992). Field study of dispersion in a heterogeneous aquifer: 1. Overview and site description. *Water Resources Research*, 28(12), 3281-3291.
- Borden, R. C., Cha, K. Y., & Liu, G. (2020). A Physically Based Approach for Estimating Hydraulic Conductivity from HPT Pressure and Flowrate. *Groundwater* In review.
- Bouwer, H. (1989). The Bouwer and Rice Slug Test—An Update a. *Groundwater*, 27(3), 304-309.
- Bultreys, T., De Boever, W., & Cnudde, V. (2016). Imaging and image-based fluid transport modeling at the pore scale in geological materials: A practical introduction to the current state-of-the-art. *Earth-Science Reviews*, 155, 93-128.
- Butler Jr, J. J., Healey, J. M., McCall, G. W., Garnett, E. J., & Loheide II, S. P. (2002). Hydraulic tests with direct-push equipment. *Ground Water*, 40(1), 25-36.
- Butler, J. J. (2005). Hydrogeological methods for estimation of spatial variations in hydraulic conductivity. In *Hydrogeophysics* (pp. 23-58). Springer, Dordrecht.
- Butler Jr, J. J., Dietrich, P., Wittig, V., & Christy, T. (2007). Characterizing hydraulic conductivity with the direct-push permeameter. *Groundwater*, 45(4), 409-419.
- By Kierano - Own work, CC BY-SA 3.0, <https://commons.wikimedia.org/w/index.php?curid=7034448>.
- Buades, A., Coll, B., & Morel, J. M. (2005, June). A non-local algorithm for image denoising. In *2005 IEEE Computer Society Conference on Computer Vision and Pattern Recognition (CVPR'05)* (Vol. 2, pp. 60-65). IEEE.
- Cleveland, R. B., Cleveland, W. S., McRae, J. E., & Terpenning, I. (1990). STL: A seasonal-trend decomposition. *Journal of official statistics*, 6(1), 3-73.
- Cressie, N. (2015). *Statistics for spatial data*. John Wiley & Sons.
- Dagan, G. (1989), *Flow and Transport in Porous Formations*, 465 p., Springer, New York.
- Dagan, G., and S. P. Neuman (1997), *Subsurface Flow and Transport: A Stochastic*

- Approach, Cambridge Univ. Press, Cambridge, UK.
19. Datta-Gupta, A., Yoon, S., Vasco, D. W., & Pope, G. A. (2002). Inverse modeling of partitioning interwell tracer tests: A streamline approach. *Water Resources Research*, 38(6), 15-1.
 20. Dekker, J. M., Sweijen, T., & Zech, A. (2020). Groundwater flow below construction pits and erosion of temporary horizontal layers of silicate grouting. *Hydrogeology Journal*, 28(8), 2821-2832.
 21. de Vries, E. T., Raof, A., van Genuchten, M. T. (2017). Multiscale modelling of dual-porosity porous media; a computational pore-scale study for flow and solute transport. *Advances in water resources*, 105, 82-95.
 22. Dietrich, P., Butler Jr, J. J., & Faiß, K. (2008). A rapid method for hydraulic profiling in unconsolidated formations. *Groundwater*, 46(2), 323-328.
 23. Dietrich, P., & Leven, C. (2009). Direct push-technologies. In *Groundwater geophysics* (pp. 347-366). Springer, Berlin, Heidelberg.
 24. Feser, M., Gelb, J., Chang, H., Cui, H., Duerwer, F., Lau, S. H., ... & Yun, W. (2008). Sub-micron resolution CT for failure analysis and process development. *Measurement science and technology*, 19(9), 094001.
 25. Fogg, G. E., Carle, S. F., & Green, C. (2000). Connected-network paradigm for the alluvial aquifer system. *Special Papers-Geological Society of America*, 25-42.
 26. Freeze, R. A., & Cherry, J. A. (1979). *Groundwater* (No. 629.1 F7).
 27. Gelhar, L. W., & Axness, C. L. (1983). Three-dimensional stochastic analysis of macrodispersion in aquifers. *Water Resources Research*, 19(1), 161-180.
 28. Geoprobe. 1992. *Geoprobe Systems® Equipment and Tools Catalog, 1992*. Salina, Kansas: Kejr, Inc.
 29. Geoprobe. 2010. *Tech Guide for Calculation of Estimated Hydraulic Conductivity (Est. K) Log from HPT Data*. Salina, Kansas: Kejr Inc./Geoprobe Systems <https://geoprobe.com/literature/tech-guide-for-estimating-k-using-hpt> (accessed May 28, 2020).
 30. Godoy, W., Pontedeiro, E. M., Hoerlle, F., Raof, A., Van Genuchten, M. T., Santiago, J., & Couto, P. (2019). Computational and experimental pore-scale studies of a carbonate rock sample. *Journal of Hydrology and Hydromechanics*, 67(4), 372-383.
 31. Held, R. J., & Celia, M. A. (2001). Pore-scale modeling and upscaling of nonaqueous phase liquid mass transfer. *Water Resources Research*, 37(3), 539-549.
 32. Hyder, Z., & Butler Jr, J. J. (1995). Slug tests in unconfined formations: An assessment of the Bouwer and Rice technique. *Groundwater*, 33(1), 16-22.
 33. Joekar-Niasar, V., & Hassanizadeh, S. M. (2012). Analysis of fundamentals of two-phase flow in porous media using dynamic pore-network models: A review. *Critical reviews in environmental science and technology*, 42(18), 1895-1976.
 34. Kechagia, P. E., Tsimpanogiannis, I. N., Yortsos, Y. C., & Lichtner, P. C. (2002). On the upscaling of reaction-transport processes in porous media with fast or finite kinetics. *Chemical engineering science*, 57(13), 2565-2577.
 35. Kim, Y., Hwang, B., & Cho, W. (2018). Development of ground freezing system for undisturbed sampling of granular soils. *Advances in Civil Engineering*, 2018.
 36. Koltermann, C. E., & Gorelick, S. M. (1996). Heterogeneity in sedimentary deposits: A review of structure-imitating, process-imitating, and descriptive approaches. *Water Resources Research*, 32(9), 2617-2658.
 37. Lapidoth, A. (2017). *A foundation in digital communication*. Cambridge University Press.
 38. Lessoff, S. C., Schneidewind, U., Leven, C., Blum, P., Dietrich, P., & Dagan, G. (2010). Spatial characterization of the hydraulic conductivity using direct-push injection logging. *Water Resources Research*, Res. 46.
 39. Leven, C., & Dietrich, P. (2006). What information can we get from pumping tests? - comparing pumping test configurations using sensitivity coefficients. *Journal of Hydrology*, 319(1-4), 199-215.
 40. Littlejohn, G. S., Concannon, M., & Wright, R. H. (1997). Engineering properties of silicate-R100 ester chemical grouts. *Ground Engineering*, 30.
 41. Liu, G., Butler, J. J., Bohling, G., Reboulet, E. C., Knobbe, S., Hyndman, D. W., & Zheng, C. (2009). A New Method for Rapid, High-Resolution Characterization of Hydraulic Conductivity: Application to Solute Transport at the MADE Site. *AGUFM, 2009*, H21B-0844.

42. Liu, G., Butler, J. J., Reboulet, E., & Knobbe, S. (2012). Hydraulic conductivity profiling with direct push methods. *Grundwasser*, 17(1), 19-29.
43. Liu, G., Borden, R. C., & Butler Jr, J. J. (2019). Simulation Assessment of Direct Push Injection Logging for High-Resolution Aquifer Characterization. *Groundwater*, 57(4), 562-574.
44. Lunne, T., Berre, T., & Strandvik, S. (1997). Proc., Recent Developments in Soil and Pavement Mechanics, Brazil, June 1997 (1997), pp. 81-102.
45. Lunne, T., Berre, T., & Strandvik, S. (1998). Sample disturbance effects in deep water soil investigations *Offshore Site Investigation and Foundation Behaviour'New Frontiers: Proceedings of an International Conference*. Society of Underwater Technology, pp. 199-220.
46. Lunne, T., Powell, J. J., & Robertson, P. K. (2002). *Cone penetration testing in geotechnical practice*. CRC Press.
47. Maliva, R. G. (2016). Direct-push technology. In *Aquifer Characterization Techniques* (pp. 383-402). Springer, Cham.
48. McCall, W., D.M. Nielsen, S.P. Farrington, and T.M. Christy. (2006). Chapter 6: Use of Direct-Push Technologies in Environmental Site Characterization and Ground-Water Monitoring. *Practical Handbook of Environmental Site Characterization and Ground-Water Monitoring 2nd New York, NY: CRC Taylor & Francis*, 346–463.
49. McCall, W., and T.M. Christy. (2010). Estimating Formation Hydraulic Conductivity (K) from HPT Q/P Ratios (abstract). *Proceedings of the 2010 North American Environmental Field Conference*. Socorro, NM: Nielsen Environmental Field School.
50. McCall, W., Christy, T. M., & Evald, M. K. (2017). Applying the HPT-GWS for Hydrostratigraphy, Water Quality and Aquifer Recharge Investigations. *Groundwater Monitoring & Remediation*, 37(1), 78-91.
51. McCall, W., & Christy, T. M. (2020). The Hydraulic Profiling Tool for Hydrogeologic Investigation of Unconsolidated Formations. *Groundwater Monitoring & Remediation*, 40(3), 89-103.
52. Owusu, Y. A. (1982). Physical-chemistry study of sodium silicate as a foundry sand binder. *Advances in colloid and interface science*, 18(1-2), 57-91.
53. Pebesma, E. J. (2004). Multivariable geostatistics in S: the gstat package. *Computers & geosciences*, 30(7), 683-691.
54. Ptak, T., Piepenbrink, M., & Martac, E. (2004). Tracer tests for the investigation of heterogeneous porous media and stochastic modelling of flow and transport—a review of some recent developments. *Journal of hydrology*, 294(1-3), 122-163.
55. Raoof, A., Hassanizadeh, S. M., & Leijnse, A. (2010). Upscaling transport of adsorbing solutes in porous media: Pore-network modeling. *Vadose Zone Journal*, 9(3), 624-636.
56. Raoof, A., Nick, H. M., Hassanizadeh, S. M., & Spiers, C. J. (2013). PoreFlow: A complex pore-network model for simulation of reactive transport in variably saturated porous media. *Computers & Geosciences*, 61, 160-174.
57. Ren, S., Yao, G., & Zhang, Y. (2019). High-resolution geostatistical modeling of an intensively drilled heavy oil reservoir, the BQ 10 block, Biyang Sag, Nanxiang Basin, China. *Marine and Petroleum Geology*, 104, 404-422.
58. Šimunek, J., van Genuchten, M.T. (2008). Modelling nonequilibrium flow and transport processes using HYDRUS Vadose Zone J., 7 (2) (2008), pp. 782-797, [10.2136/vzj2007.0074](https://doi.org/10.2136/vzj2007.0074).
59. Sun, H., & Koch, M. (2014). Under-versus Overestimation of Aquifer Hydraulic Conductivity from Slug Tests. In *ICHE 2014. Proceedings of the 11th International Conference on Hydroscience & Engineering* (pp. 327-336).
60. Tang, Y. Q., & Yan, J. J. (2015). Effect of freeze-thaw on hydraulic conductivity and microstructure of soft soil in Shanghai area. *Environmental Earth Sciences*, 73(11), 7679-7690.
61. Taylor, M. L., Cubrinovski, M., & Haycock, I. (2012, April). Application of new 'Gel push' sampling procedure to obtain high quality laboratory test data for advanced geotechnical analyses. In *2012 New Zealand Society for Earthquake Engineering Conference*. Christchurch, New Zealand, NZSEE. Paper No. 123, 1-8.
62. Thornton, D., Ita, S., & Larsen, K. (1997). Broader use of innovative ground water access technologies. In *Proceedings of Superfund 18th Conference*, Vol. 2, pp. 639-646.
63. Umehara, Y., Chiaro, G., Kiyota, T., Hosono, Y., Yagiura, Y., & Chiba, H. (2015). Effectiveness of

- 'gel-push'sampling technique to retrieve undisturbed sandy specimens for liquefaction test. In *Proceedings of 6th International Conference on Earthquake Geotechnical Engineering*, Christchurch, New Zealand, November 2015.
64. Van der Stoep, A. E. C. (2001). Grouting for pile foundation improvement. PhD Thesis, Tech. Univ. Delft, The Netherlands.
 65. White, R., & Kelly, S. (2020). Correlative, Multi-scale, Lab-based X-ray Tomography: From Millimeters to Nanometers. *Microscopy and Microanalysis*, 26(S2), 1002-1003.
 66. Wiggers, A., Sanders, M., Niemeijer, H., Tonneijck, M. (2019). POV Piping Portaal. *POV Piping*, Hoogwaterbeschermingsprogramma.
 67. Wildenschild, D., & Sheppard, A. P. (2013). X-ray imaging and analysis techniques for quantifying pore-scale structure and processes in subsurface porous medium systems. *Advances in Water Resources*, 51, 217-246.
 68. Yoshimi, Y., Tokimatsu, J., & Ohara, A. N. (1994). In situ liquefaction resistance of clean sands over a wide density range. *Geotechnique*, 44(3), 479-494.
 69. Zeiss microscopy on YouTube. <https://www.youtube.com/watch?v=9lgh07h8fvg>
 70. ZEISS Xradia Versa Product Information. <https://www.zeiss.com/microscopy/us/products/x-ray-microscopy/zeiss-xradia-610-and-620-versa.html>